1-2024

Trace and rare earth elements analysis of Oligocene and Miocene diamictites in the Cape Roberts Project, Ross Sea, Antarctica

Celina Flores Garza

Abstract

The West Antarctic Ice Sheet is a major contributor to global sea level rise, yet its origin and dynamics are poorly known. The geochemistry of 35 diamictite samples from the CRP-1 and CPR-2A cores recovered by the Cape Roberts Drilling Project in the Ross Sea, Antarctica is evaluated to understand glacial sedimentation and flow paths during the Oligocene and Miocene, a period of warmer than present climate in the past. The major hypothesis to be tested is if the early Miocene ice sheet advance was the first major West Antarctic ice advance in the Ross Sea. The provenance of older Oligocene diamictites, present below this early Miocene stratigraphic level, will be analyzed to trace glacially transported sediment to a West Antarctic or an East Antarctic source. The project implies that if the Oligocene diamictites show a West Antarctica signature, a major ice sheet advance took place before the early Miocene, as proposed in previous geophysical research.

Whole rock analysis of diamictite samples is performed on an Inductively Coupled Plasma Mass Spectrometer (ICP-MS). This kind of analysis allows the interpretation of a range of elemental ratios that indicate specific sources to determine the sediment provenance for each diamictite sample. In addition, grain-size distributions (Martin and Passchier, 2010) will be used to assess the depositional setting of the diamictites. Results show a main East Antarctic provenance with a contribution from a West Antarctic source, suggesting the presence of a West Antarctic Ice Sheet advance during the Oligocene. These results enhance our understanding of ice sheet evolution and dynamics in Antarctica through warmer periods in the past and lead to better projections for global warming and rising sea levels worldwide.

MONTCLAIR STATE UNIVERSITY

Trace and Rare Earth Elements analysis of Oligocene and Miocene diamictites in the Cape Roberts Project,

Ross Sea, Antarctica

By

Celina Flores Garza

A Master's Thesis Submitted to the Faculty of

Montclair State University

In Partial Fulfillment of the Requirements

For the Degree of

Master of Science

January 2024

College of Science and Mathematics

Department of Earth and Environmental Studies

Thesis Committee:

Dr. Sandra Passchier

Thesis Sponsor

Dr. Matthew Gorring

Committee Member

Dr. Clement Alo

Committee Member

TRACE AND RARE EARTH ELEMENTS ANALYSIS OF OLIGOCENE AND MIOCENE

DIAMICTITES IN THE CAPE ROBERTS PROJECT, ROSS SEA, ANTARCTICA

A THESIS

Submitted in partial fulfillment of the requirements

For the degree of Master of Science

by

Celina Flores Garza

Montclair State University

Montclair, NJ

2024

Acknowledgments

First, I want to express my gratitude to Dr. Sandra Passchier, my thesis sponsor. I appreciate the opportunity she provided me to contribute to this incredible project, her ongoing guidance, patience, and support, and for being more than just an advisor through this process. I would also like to thank my thesis committee members, Dr. Matthew Gorring and Dr. Clement Alo for all their help and support. Also, thanks to Dr. Xiaona Li for all her assistance and instruction in the ICP-MS methods. Additionally, thanks to everyone participating in the Cape Roberts Project for their contribution of funds and information to support this project.

Special appreciation goes to Victoria Hojnacki for her valuable advice, support, and friendship during the stressful process of writing this thesis; Linda Martin for her assistance in the grain size preparation; Archana Prasad for her grammatical writing input and insistence on taking breaks when things got too stressful; and to my dear Latinas: Diana Cuevas, Victoria Aceves, Marilu Amezcua, and Julieta Ayala, for always cheering me up when I wanted to quit and for being my overseas family.

I want to extend special thanks to my parents, Ariel and Cecilia, for supporting my dreams in a country far from home, and for teaching me to be disciplined, hard-working and always to dream big. Additionally, I express gratitude to my beloved husband, Jeff Vreeland, for consistently reminding me that with diligence and dedication, anything is achievable. I am thankful for his unconditional love, infinite patience, and support during my master's program.

Table of Contents

List of Tables

List of Figures

Introduction

The Antarctic continent is positioned at the South Pole, secluded from the rest of the world. Despite minimal life, the continent's ice sheets continually exhibit dynamic processes, either advancing or retreating, and transporting sediments toward the coasts. The thick ice covering the Antarctic continent complicates the geological exploration and understanding of its geology. Seismic data and available drill cores are also very limited, and few studies have been carried out on the available core material. For this reason, the evolution of the Antarctic ice sheets through past warm periods in the past is still poorly known.

In 1998, a multinational group was established to obtain a continuous stratigraphic record from beneath western McMurdo Sound in the Ross Sea sector of Antarctica by drilling overlapping drill holes through a sedimentary succession that intersects the sea floor at Roberts Ridge, as part of the Cape Roberts Project (CRP) (Cape Roberts Science Team, 1998). The project was named after Cape Roberts, a small promontory 125 km northwest of the U.S. McMurdo Station and N.Z. Scott Base, which was the staging point for offshore drilling (Florindo et al. 2005).

Previous studies have used the cores collected by CRP to create age models and long-term stratigraphic records of environmental change: Florindo et al. (2005) determined the magnetostratigraphic chronology of the late Eocene to early Miocene sediments from the cores CRP-1, 2, and 3. Passchier and Krissek (2008) studied the major element geochemistry of the mud rocks of the drill cores CPR-1 and 2A to evaluate the continental paleotemperatures and weathering history of the area. Passchier (2004) previously analyzed samples from Southern Victoria Land to evaluate the provenance and stratigraphic relations of the Sirius Group in the Transantarctic Mountains.

Also, studies have been done in the Ross Sea with different methods than drilling cores and on other drill cores than CRP. Marschalek et al. (2021) provided geochemical and petrographic data proving the largest West Antarctic Ice Sheet (WAIS) existed and expanded across the continental shelf during the early Miocene from a drill site on the outer shelf of the Ross Sea. On the other hand, Sorlien et al. (2007) documented the first seismic stratigraphic evidence of marine Oligocene grounded ice located far from an elevated source in Marie Byrd Land, placing the initiation of the WAIS during the late Oligocene. Because of these contrasting hypotheses, more research is needed about the sediment provenance of diamictites in the Ross Sea to understand the ice sheet advance in the West Antarctic during the Oligocene and Miocene.

Diamictites are originated predominantly from mechanical erosion of the rock types exposed along the path of glacial drainage. If these diamictites' geochemistry is analyzed, the sediments reflect the average composition of the upper crust in the glaciated area (Passchier, 2004). Diamictites present in the CPR succession can tell us about the history of West Antarctica during the Oligocene and Miocene. The annual sea surface temperature in the Antarctica region during the Oligocene to early Miocene was a range of 3-6°C (Duncan et al., 2022), which is higher than the current sea surface average temperature of -1.8 °C measured at McMurdo Station in the Ross Sea (NSF, 2020). Knowing the provenance of these diamictites could contribute valuable information to understand better the paleoclimatic and glacial dynamics during this period.

The objective of this study is to analyze trace and Rare Earth Elements of 35 diamictites using ICP-MS to test the hypothesis by Sorlien et al. (2007) that the first WAIS advance in the Ross Sea happened during the Oligocene.

Cape Roberts Project

The Cape Roberts Project (CRP) is a collaboration among multiple nations, including Australia, Germany, Italy, the Netherlands, New Zealand, the United Kingdom, and the United States. The primary emphasis of the project is to obtain a continuous core through 1200 m of strata on the western side of McMurdo Sound, Antarctica to investigate the Cenozoic climatic and tectonic history of the region (Cape Roberts Project, 1999).

CRP-1 and CRP2-2A location

The sites for CRP-2 and CRP-2A, 14 km east of Cape Roberts, were selected to overlap the early Miocene strata cored in nearby CRP-1 and to sample deeper into the east-dipping strata near the western margin of the Victoria Land Basin to investigate Paleogene climatic and tectonic history. CRP-2 was cored from 5 to 57 meters below sea floor (mbsf), with a deviation resulting in CRP-2A being cored at the same site. CRP-2A reached down to 624 mbsf and to strata with an age of 33-35 Ma. The drilling took place from October 16th to November 25th, 1998, on 2.0 m of sea ice and through 178 m of water (Fig. 1).

During the drilling phase of the project, weather observations were recorded at the Cape Roberts Camp. Average daily temperatures rose from -25°C at the start of drilling in early October to -5°C at the end of drilling in late November. Winds were generally light; the maximum measured wind was 32 knots (Cape Roberts Project, 1999).
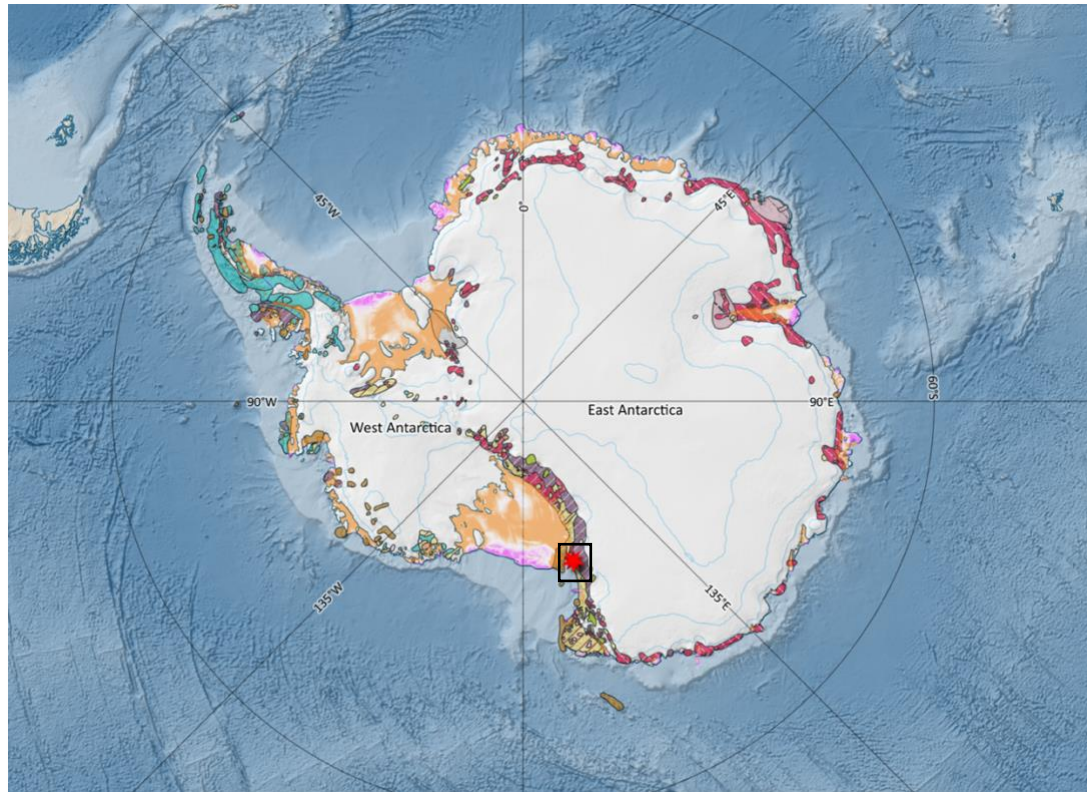
LEGEND
Location
★ CRP
Geology

ARCHEAN - Amphibolite facies metamorphic rocks
ARCHEAN - Granitoids
ARCHEAN - Granulite facies metamorphic rocks
CARBONIFEROUS - Granitoids
CENOZOIC - Sedimentary rocks
CENOZOIC - Volcanic rocks and minor intrusives; includes active volcanoes
DEVONIAN - Granitoids
DEVONIAN - Volcanic rocks
LOWER JURASSIC - Tholeiitic volcanic rocks
MESOZOIC - Granitoids
MESOZOIC - Metamorphic rocks
MESOZOIC - Metamorphic rocks / Granitoids
MESOZOIC - Sedimentary rocks
MESOZOIC - Sedimentary rocks / Granitoids
MESOZOIC - Volcanic rocks
MESOZOIC - Volcanic rocks / Granitoids
MESOZOIC - Volcanic rocks / Metamorphic rocks
MESOZOIC - Volcanic rocks / Sedimentary rocks
No data entered - Intrusive rocks
PALEOZOIC - Granitoids
PALEOZOIC - Sedimentary and volcanic rocks including metamorphosed examples
PHANEROZOIC - Continental Sedimentary rocks
PHANEROZOIC - Metamorphic rocks / Sedimentary rocks
PHANEROZOIC - Sedimentary and volcanic rocks including metamorphosed examples / Granitoids
PHANEROZOIC - Sedimentary rocks
PROTEROZOIC - Granitoids including chamockites
PROTEROZOIC - Granitoids including chamockites / Sedimentary and volcanic rocks including metamorphosed examples
PROTEROZOIC - High grade metamorphic rocks
PROTEROZOIC - High grade metamorphic rocks/ Granitoids including chamockites
PROTEROZOIC - Mafic intrusives - gabbro
PROTEROZOIC - Metasediments - low metamorphic grade
PROTEROZOIC - Metasediments - low metamorphic grade / Sedimentary and volcanic rocks including metamorphosed examples
PROTEROZOIC - Volcanic rocks

Figure 1. Location of CRP succession in the Ross Sea, West Antarctica. Created in QGIS using Quantarctica database with geological map of 2021.

Regional Geology

Antarctica is approximately 14.2 million square kilometers with an average of 2,160 meters of thick ice covering about 98 percent of the land. The continent is comprised of two primary continental blocks: East Antarctica and West Antarctica. The East Antarctic crust comprises ancient cratonic and orogenic material with highly variable magnetic signatures. The West Antarctic crust comprises immature sedimentary rocks, magmatic arc material, and extended, thinned continental blocks with high magnetic anomalies due to arc magmatism (Tinto et al. 2019).

The development of the East Antarctic craton was initiated in the Archean and concluded in the Cambrian (Anderson, 1999). Precambrian terranes were accreted onto Archean nuclei during several collisional events, namely the Grenville (~1.0 Ga) and Pan-African (~600-500 Ma) orogens, leading to the assembly of Rodinia and Gondwana respectively (Boger, 2011). In the early stages of Gondwana's formation, Antarctica occupied a latitude similar to present-day South America (Anderson, 1999). Early to middle Jurassic rifting eventually led to the separation of Africa from Madagascar and East Antarctica. The ongoing process of rifting and Gondwana's fragmentation resulted in Antarctica becoming isolated in the southern polar region. The opening of ocean gateways as continents separated contributed to a shift from warmer to colder climates (Kennett, 1997). The formation of Antarctica's ice sheets began at approximately 34 Ma, around the Eocene-Oligocene boundary, ultimately covering the entire continent (Anderson, 1999).

The Transantarctic Mountains (TAM) acts as a boundary, separating the ancient ~200 km-thick cratonic lithospheres of East Antarctica from the thinned crust and warm upper mantle province known as the West Antarctic Rift System (WARS) (Goodge, 2020). The uplift of the

present-day TAM predominantly occurred in the late Mesozoic and early Cenozoic, coinciding with extension in the WARS. The origins of the modern TAM are subject to debate: for instance, Brink et al. (1997) proposed a plate reorganization in the Southern Ocean, which may have induced transtensional motion between East and West Antarctica. This motion could have led to the formation of a fault zone that decoupled the lithosphere, resulting in rapid rock uplift. On the other hand, Bialas et al. (2007) proposed a plateau hypothesis suggesting that the WARS constitutes the central expanse of elevated terrain with thicker-than-normal crust. In this scenario, the TAM forms one edge of the plateau, while Gondwana comprises the opposite edge, having rifted away after the breakup of Gondwana. Tinto et al. (2019) proposed with a gravity-derived density model that TAM is not the boundary that divides East and West Antarctica. Instead, the major tectonic boundary is located in the middle of the Ross Sea continental shelf based on the difference in density of the two sides revealed in the column of rock present across this region.

West Antarctica is a geologically complex region that has formed between East Antarctica and the Pacific Ocean. Three broad geological provinces are identified: the Weddell Sea sector, the WARS, Marie Byrd Land and Ross Embayment, and the Antarctic Peninsula and Thurston Island. The Weddell Sea sector includes the oldest rocks in West Antarctica associated with back-arc extension in the Weddell Sea rift system. WARS, Marie Byrd Land and Ross embayment originated as a subducting margin from the East Antarctic orogen. Subduction came to a halt during the Cretaceous, coinciding with substantial crustal extension and the formation of a wide rift basin. The Antarctic Peninsula and Thurston Island serve as examples of a continental margin magmatic arc, preserving a geological record of the magmatic flare-ups (Jordan et al. 2020).

The Ross Embayment comprises the Ross Sea and the Ross Ice Shelf, featuring three sedimentary basins: The Eastern Basin, the Central Trough, and the Victoria Land Basin (VLB) (Fitzgerald et al. 1986). The basins in the Ross Sea have been shaped by two primary crustal events.

The first event involved non-magmatic rifting across most of the Ross Sea, likely linked to the Gondwana breakup in the late Mesozoic. As subduction along the western margin of Antarctica ceased, Mesozoic calc-alkaline activity gradually transitioned in the Cenozoic to more alkaline volcanism associated with an extensional regime (Baker et al. 1977). The second event, linked to tectonic activity limited to the VLB, commenced in the late Eocene-early Oligocene. This event gave rise to rift-related volcanism that persists to the present day (Cape Roberts Project, 1999).

Geochemical signatures of West and East Antarctica

Despite significant efforts made over the past decades to investigate continental crustal structure in various regions worldwide, the Antarctic continent lacks comprehensive geological data coverage (Baranov et al. 2021). The Antarctic continent is characterized by terranes of varying ages, from early Archean blocks in East Antarctica to the Cenozoic crust in West Antarctica. The crustal blocks in West Antarctica are relatively young, with ages of less than 1.0 billion years, while East Antarctica is predominantly composed of Proterozoic blocks, including some Archean blocks (Mikhalsky, 2008). This diversity in structure reflects the crust's origin and tectonic history, influencing its physical and geochemical properties.

The geochemical composition of East Antarctica closely resembles that of an ancient upper continental crust. This provenance consists of old igneous, metamorphic, and sedimentary

terranes that have been influenced by intracrustal geochemical differentiation (McLennan et al., 1993). The geochemistry of sediments derived from this component is normally characterized by a significant negative Eu anomaly and enrichment of Light Rare Earth Elements (LREE).

In contrast, West Antarctica has a similar geochemical composition to a younger crust. This provenance component represents young mantle-derived volcanic and plutonic igneous rocks from island and continental arcs. Significant negative Eu anomalies are absent, and trace element compositions show less LREE enrichment than an old upper crustal source and lower ratios of incompatible to compatible elements such as Th/Sc.

Subglacial Processes

As stated previously, the diamictites' geochemistry is analyzed, because these sediments reflect the average composition of the upper crust in the glaciated area (Passchier, 2004). The glacial environment is one of the more difficult to summarize because the glaciers can affect depositional processes both glaciomarine and glacioterrestrial, and there are many sub-environments in these settings.

The formation of glacial ice occurs as snow accumulates and, at certain depths, experiences successive cycles of partial melting, refreezing, and recrystallization. Glacier ice moves under the influence of gravity in response to vertical and shear stresses. The glacier movement rate depends on the glacier's surface slope, the thickness of the ice, and the thermal regime of the glacier, which is the temperature of the ice that affects not only the rate of movement but also the capacity of the ice to erode, transport and deposit sediment.

Cold-based glaciers are typical in cold, high-latitude regions, where the base of the ice is below the pressure melting point and where there is no water present. These glaciers move very

slowly by internal deformation at rates of a few meters per year and are ineffective in eroding

bedrock. As a result, cold-based glaciers cannot move much sediment and are ineffective

geomorphic agents. Warm-based glaciers operate near the pressure melting point and advance

through a combination of gradual deformation and sliding atop thin water films at the base of the

ice. Some freezing of the water occurs in the lee of bedrock irregularities creating an effective

method to incorporate debris into the ice base (Boulton, 1996). Warm-based glaciers are highly

abrasive and can carve into bedrock and transport large amounts of freshly broken clastic

sediments.

The most common sediment type ascribed to glacial processes is an extremely poorly sorted

deposit composed of mud, sand, gravel, and boulders. Glaciers can transport and deposit poorly

sorted mixtures of clasts and matrices in several ways. This poorly sorted material was identified

and given the name "diamictites" and diamictites that are directly deposited by ice are named

"tills".

Several processes are responsible for the deposition of subglacial tills beneath warm-based

ice, including melt-out, lodgment, and deformation. Many successions are the result of not one,

but several processes. Glacial processes leave a unique structural imprint, offering valuable

information to differentiate between subglacial deposits and other processes affected by glacial

ice.

The formation of melt-out till can occur through the release of basal and englacial debris

as glacial ice undergoes in-place melting. Till forms as debris released from the ice either

subglacially or supraglacially. Melt-out tills may show foliation or banding, that reflects the

textural and compositional variability of debris contained in the ice. In lodgment processes, tills

can also form by the melt-out of debris from the base of moving ice and smearing onto the

substrate. This produces lenticular beds of dense, consolidated diamict that may contain sub-horizontal shear planes and slickenside surfaces. Bullet-shaped boulders are also common in lodgment tills. In deformation processes, an effective till-forming process is the subglacial mixing of pre-existing sediment within a subglacial traction layer comprising water-saturated debris. This produces thick accumulations of deformation by subglacial shearing and mixing of pre-existing sediments and sediments melted out from the glacier (van der Meer et al. 2003). The processes mentioned before are the suggested mechanisms responsible for the formation of the diamictites observed in the CRP succession.

Methods and Materials

Sample Selection

The selection of samples was determined by the presence of diamictites, characterized by coarse angular to well-rounded, clastic fragments embedded in a fine-grained matrix. These sedimentary mixtures are eroded from their source, transported by the expanding ice sheet, and deposited into the basin.

The selection of intervals was influenced by the identification of shear fabrics interpreted to be formed by grounded ice over the drill site. The sample intervals were established through observations made during the initial drilling conducted by the Cape Roberts Project. The depths in the original CRP-1 and CRP-2A reports were listed in meters below seafloor (mbsf) for each drill site, then converted to cumulative meters depth (cmd) by subtracting 43.55 m to depths in interval 1 and adding 45.42 m to depths in interval 2 and 3 for a better understanding of the composite depth for the proposed age model. The conversions from mbsf to cmd were based on Florindo et al. (2005) cumulative depths for the CRP Eocene-Miocene succession.

- Interval 1 samples in CRP-1 were chosen approximately every 2 meters (119 – 140 mbsf, 75.45 – 96.45 cmd).

- Interval 2 samples in CRP 2-A were chosen approximately every 1 meter (298 – 306 mbsf, 343.42 – 351.42 cmd).

- Interval 3 samples in CRP 2-A were chosen approximately every 0.5 meter (437 – 443 mbsf, 482.42 – 488.42 cmd).

Age model

Detailed magnetostratigraphic age models have been developed for the CRP succession. Originally, the CRP succession was thought to contain a 1472-m cumulative record of late Eocene-early Miocene sediment in three sites, CRP-1, CRP-2/2A, and CRP-3. Florindo et al. (2005) conducted a magnetostratigraphic study, creating an updated model for the CRP succession. The correlation to the geomagnetic polarity time scale (GPTS) of Cande and Kent (1995) and Berggren et al. (1995) was constrained by several $^{40}Ar/^{39}Ar$ and $^{87}Sr/^{86}Sr$ ages obtained from both in situ and reworked materials by a new Antarctic siliceous microfossil zonation (Lavelle, 2000, Wilson et al., 2002) and by calcareous nannoplankton biostratigraphy (Watkins et al. 2001) dividing the CRP succession into 4 subdivisions based on the composite depth.

Subdivision 1 (0.00-175.69 cmd): early Miocene

An $^{87}Sr/^{86}Sr$ date (18.62±0.22 Ma) obtained from a solitary coral (Lavelle, 2000) at a depth of 81.67 cmd in CRP-2 suggests a unique correlation for magnetozone 1N1 with Chron C5En. Additionally, a $^{40}Ar/^{39}Ar$ age (21.44 ± 0.05Ma) for an ash horizon at 158 cmd constrains a correlation of the base magnetozone 2N4 to Chron C6An.2n (Wilson et al. 2000).

Subdivision 2 (175.69-352.02 cmd): Oligocene-Miocene boundary

The Oligocene-Miocene boundary occurs at the C6Cn.2r-C6Cn.2n polarity transition which lies at a depth of 229.12 cmd in the CRP succession. The correlation is established through four $^{87}Sr/^{86}Sr$ dates, two from in situ articulated bivalves and two from reworked bivalve fragments, and two biostratigraphic datums. The resulting magnetostratigraphy is in turn calibrated by $^{40}Ar/^{39}Ar$ dates on two tephra layers at 239 and 325 cmd (23.98±0.13 and 24.22±0.03Ma, respectively).

Subdivision 3 (352.07-488.41 cmd): late Oligocene

Wilson et al. (2000) encountered challenges in correlating the normal polarity of magnetozone 2N6 with the GPTS in the late Oligocene due to various factors, including numerous unconformities, a lack of independent age control, and the intricate nature of the GPTS. Florindo et al. (2005) proposed this interval to be of late Oligocene age.

Subdivision 4 (488.41-1472.37 mbsf): late Oligocene – early Oligocene

The dominance of reverse polarity, along with diatom and nannofossil biostratigraphic constraints and five $^{87}Sr/^{86}Sr$ dates, one from an in situ articulated bivalve and the others from reworked bivalve fragments, suggests that the interval between 669.57 and 1007.57 cmd correlates with magnetozone 3R1 and part of C12r (Florindo et al., 2001). Thus, the overlying interval (488.41-669.56 cmd) of complex polarity must correlate with Chron C12n and/or younger subchrons. $^{87}Sr/^{86}Sr$ dates from in situ articulated bivalves at 490.46 (29.4±0.5 Ma) suggest that the lower part of magnetozones 2R6, 2N7 to 2N12 correlate with chrons C10n.1r-C12n (Wilson et al. 2000).

Based on the Age Model proposed by Florindo et al. (2005), interval 1 was deposited between the solitary coral and the tephra layer in subdivision 1, dated ~18-21 Ma. Interval 2 was

deposited between the two tephra layers present in the lowermost part of subdivision 2, dated

~24 Ma. While interval 3 was deposited in the bottom part of subdivision 3, dated ~27-29 Ma. A

total of 35 samples were chosen from the CRP 1 and CRP-2A core: 12 samples between 119 -

140 mbsf, 75.45 – 96.45 cmd, 12 samples between 298 - 306 mbsf, 343.42 – 351.42 cmd, and 11

samples between 437 - 443 mbsf, 482.42 – 488.42 cmd.

Interval 1 was taken from CRP-1, the lithostratigraphic sub-unit (LSU) 6.3. (Fig. 2) LSU

6.3 is a sequence of clast-poor to clast-rich diamictite. The rock is lithified but appears

uncemented. This unit is uniformly massive with thicknesses of several meters, although

laminae, thinly formed beds, lenses, and wispy parting of claystone, siltstone, and sandstone

occur at some levels. At 133.57-133.77 mbsf a prominent clastic dyke extends from a siltstone

horizon below. Clasts are angular to well-rounded and include granite, dolerite, other volcanic

rocks, and lesser proportions of soft sediment clasts. Fossil fragments occur rarely (Cape Roberts

Project, 1998).

Interval 2 was taken from CRP-2A, LSU 10.1. (Fig. 3) This sub-unit contains several

lithologies interbedded and deformed at a variety of scales. Lithologies include: 1) muddy to

sandy, clast-poor to clast-rich diamictite, 2) muddy fine sandstone, locally with dispersed clasts,

3) very fine sandy mudstone, and 4) moderately sorted fine to very coarse sandstone.

Interval 3 was taken from CRP-2A, LSU 12.4. (Fig. 3) The upper 18 m of

lithostratigraphic LSU 12.4 are composed of a variety of sandstone types of interbedded

sandstone intervals that are 1 - 3 meters thick and lie between diamictite beds that are 40-80 cm

thick. The sandstones range from massive to ripple cross-laminated and cross-bedded. A clast-

poor sandy to muddy diamictite forms the basal 5.12 m of this unit.
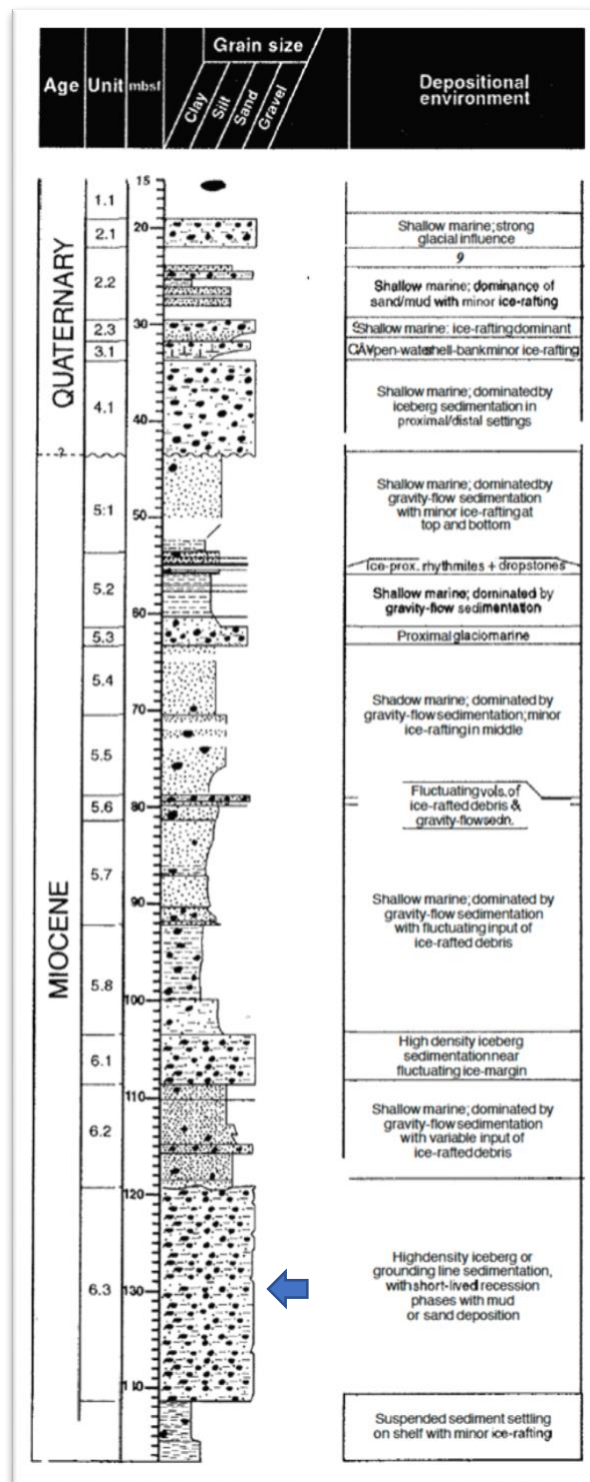
Figure 2. Lithology from CRP-1. Blue arrow shows where samples were taken from.
Modified from Cape Roberts Project (1998).
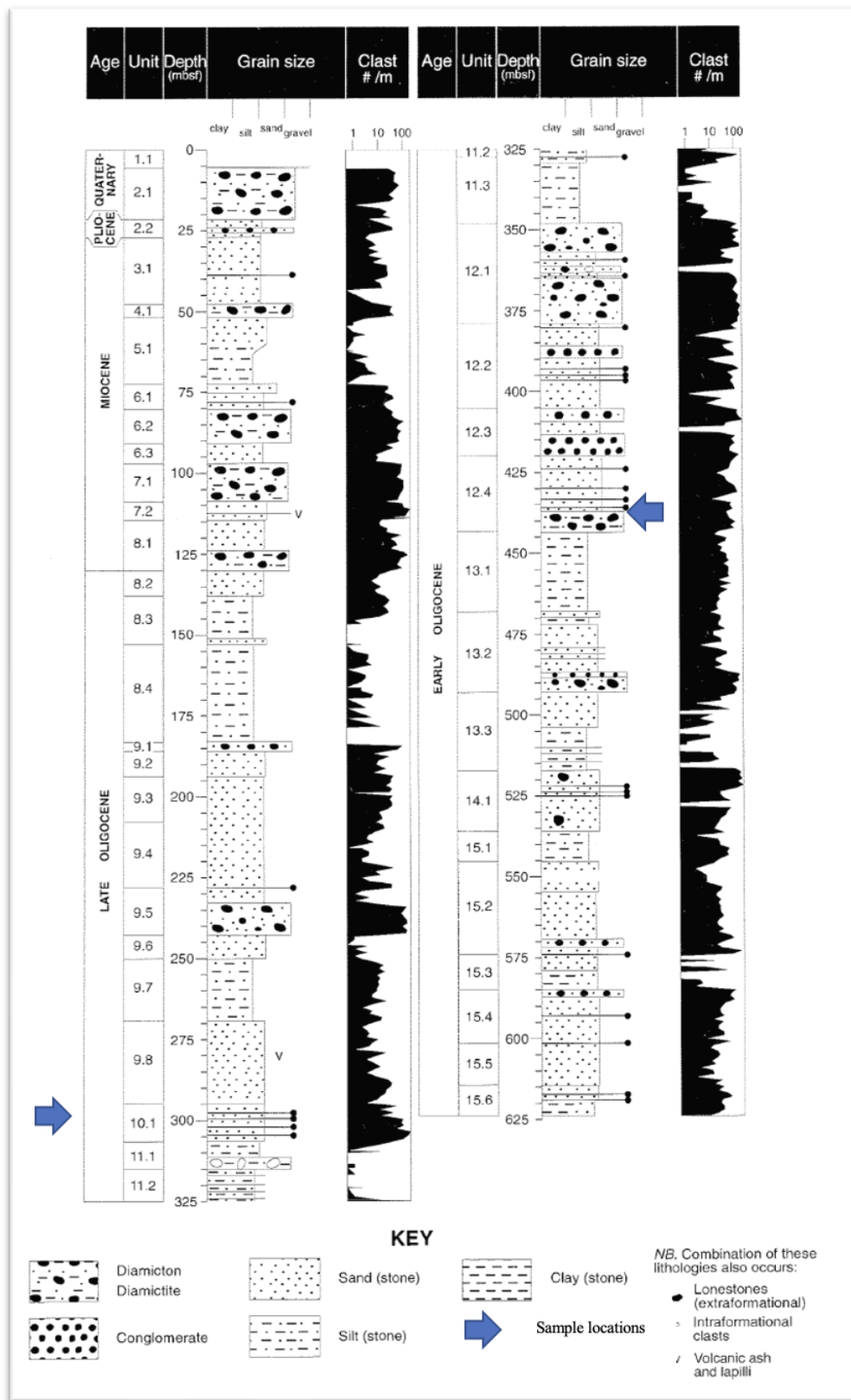
Figure 3. Lithology from CRP-2/2A. Blue arrows show intervals where samples were taken from. Modified from Cape Roberts Project (1999).

Geochemical Analysis

The objective of studying fine-grained diamictites is to determine the provenance of the deposited material. This can be accomplished by plotting various chemical ratios that may be indicative of the source regions.

This study uses samples that were already disaggregated for ICP analysis (Martin and Passchier, 2010) as described in Hansen (2011). The disaggregation involved breaking off approximately 1/3 of each consolidated sediment sample and wet crushing it with a mortar and pestle. The disaggregated samples were subsequently wet-sieved using deionized water through a 63-µm sieve and collected into a sealed plastic container. The blend of fine fraction mixture was left to settle for a week before being decanted and dried. Where necessary, the decanted water was centrifuged to guarantee the absence of sediment loss. The dried-out sediment was stored in 50-mL glass storage vials. For this study, between 0.0995 and 0.1005 grams of sample from each of the vials was weighed and mixed with approximately 0.3980 – 0.4020 grams of lithium metaborate flux. Weights were documented for each sample, and subsequently, the sample and the flux were meticulously mixed before being transferred into a graphite crucible. A corresponding blank, consisting solely of the flux, was prepared for each set of samples.

Following that, the samples were placed into the furnace, which had been pre-set to 1050°C for 30 minutes. A Teflon beaker with a stir rod was then positioned on the balance, its weight tared, and approximately 50 mL of 7% nitric acid was measured out and poured into the beaker. The weight of the acid was documented, and the Teflon beakers were set aside until the diffusion process was concluded.

After the samples underwent fusion, the crucibles were removed from the furnace, and the resulting molten bead was delicately moved into the acid. Upon contact with the acid, the

molten bead fragmented, facilitating easier dissolution. The beakers were then positioned on stirring plates, allowing the shattered beads to fully dissolve. Subsequently, once the beads were dissolved, the samples were filtered using Whatman 540 filter paper directly into a 60 mL Nalgene bottle.

Two 6.5 mL aliquots of solution previously prepared were pipetted into an empty 60 mL Nalgene bottle, and its weight was documented. Then, about 50 mL of 2% nitric acid was added, and its weight was also recorded. All the samples were then stored in a refrigerator to mitigate the risk of evaporation and slow down chemical reactions. Immediately before ICP-MS analysis, 0.5 mL of each sample was pipetted into a test tube and further diluted by adding 9.5 mL of 2% nitric acid. Trace (Ni, Cr, Sc, V, Rb, Ba, Sr, Zr, Y, Nb) and Rare Earth (La, Ce, Pr, Nd, Sm, Eu, Gd, Tb, Gd, Dy, Ho, Er, Tm, Yb, and Lu) elemental abundances were determined. Calibrations were obtained using ten USGS rock standards (DNC-1, BHVO-2, G-2, W-2, BCR-2, GSP-2, QLO-1, AGV-2, BIR-1, and RGM-1) that were prepared using the same methods, whereas MAG-1 and SCO-1 standards were prepared to be measured as unknowns. Five analytical procedural blanks were prepared identically to the previously mentioned samples, with the exception that only $LiBO_2$ flux was added and dissolved.

Internal standards MAG-1 and SCO-1 were used to calculate accuracy and precision for all measurements. The precision of the internal standards MAG-1 and SCO-1 was less than 2% of the average while the accuracy was calculated to be greater than 95%.

The identification and concentration of trace and Rare Earth Elements were determined with the utilization of the Thermo Scientific iCap Q ICP-MS at Montclair State University. ICP-MS is a common method for analyzing liquid samples. In this process, a sample solution was transformed with argon gas to create a fine aerosol mist. The mist travels through a quartz tube

where sample decomposition occurs, leading to ionization. Ionis are extracted and directed to the

mass spectrometer. The mass-to-charge ratio separation in the mass spectrometer allows specific

ions to reach the detector, enabling precise concentration measurements in the ICP-MS.

Grain Size Distribution

Analyzing grain size can aid in identifying the depositional environment of sediments.

The primary goal of this investigation was to characterize diamictites during the Miocene and

Oligocene. Diamictites exhibit shear fabrics, signifying that the sediments were deposited in a

setting of subglacial deformation during the advance or retreat of the ice sheet. Studying the

grain size of the diamictite intervals allows for the assessment of whether the depositional

environment was consistent or underwent changes during sediment deposition.

The data used here is from Martin and Passchier (2010). Preparation for particle size

analysis was adapted from Appendix C of Konert and Vandenberghe (1997) and as described in

Hansen (2011).

Approximately 100 – 200 mg of each sample was broken off, gently tapped with a

hammer, and transferred to a 250 mL beaker with approx. 20 mL of water. A 10-mL aliquot of

30% H_2O_2 was combined with the sample, covered with a watch glass, and left overnight for

oxidation. The sample was then subjected to a sonicator to aid in breaking down larger

fragments. Later, the sample and H_2O_2 mixture were heated to guarantee the completion of the

reaction, with deionized water used to rinse the beaker walls to prevent sample loss. When the

reaction concluded, 5 mL of 10% HCl was added and left on the hot plate for at least 10 minutes.

The use of H_2O_2 and HCl ensured the dissolution of any organic material. The samples were

centrifuged at 1500 RPMs for 30 minutes, decanted, and the process was reiterated. Following

two rounds of centrifugation, the samples were reintroduced into their initial beakers, and heated

with sodium pyrophosphate ($Na_4P_2O_7*10H_2O$).

The sample was then viewed under a microscope and any portions displaying clumps

underwent sonification for one hour. In cases where sonification did not eliminate large clumps,

a mortar, and pestle were employed to gently tap on the larger clumps. Following this, the

sample was returned to the sonificator to further break down the clumps. Particle size

distributions were assessed using the Malvern Mastersizer 2000 laser diffractometer with a

Hydro 2000MU pump accessory at Montclair State University. The Mastersizer pump propeller

was adjusted to 2200 rpm to generate adequate turbulence, ensuring the suspension of both

coarse and fine sediments. Sample obscuration was kept between 15 and 30%.

Results

Geochemical Results

Elemental Enrichments

To better constrain provenance at the CRP-1 and CRP-2A sites, Trace and Rare Earth Elements (REEs) were utilized to create elemental spider diagrams. REE enrichment was calculated through the normalized ppm of elements in each sample divided by the Post-Archean Average Australian Shale (PAAS) (Taylor and McLennan, 1985), average Chondrite (McLennan, 1989), and Upper Continental Crust (UCC) (Taylor and McLennan, 1981). The values were then scaled logarithmically: values above 1 indicate enrichment, whereas values below 1 indicate a depletion of that element in the sample.

Elemental spider diagrams were created for REEs normalized to the PAAS, average Chondrite, and UCC, and the data for CRP-1 and CRP-2A samples are given in Tables 1, 2, and 3. On normalized diagrams, europium enrichment in comparison to other REEs is identified as a positive Eu-anomaly. The samples exhibit notably consistent REE patterns across intervals for PAAS, average Chondrite, and UCC. Under PAAS normalization (Fig. 4), most samples display a depletion in the Light Rare Earth Elements (LREEs), accompanied by a positive Eu anomaly. Additionally, there is a relatively flat profile for Gd, Tb, and Dy with slight depletion for Ho, Er, Tm, Yb, and Lu. On the other hand, under Chondrite normalization (Fig. 5), the samples reveal enrichment in the LREEs, a presence of a weak Eu anomaly, and a relatively low enrichment in the Heavy Rare Earths (HREEs) except for Yb. Similarly, under UCC normalization (Fig. 6), the samples show enrichment in the LREE, the presence of a positive Eu anomaly, and enrichment in the HREE.
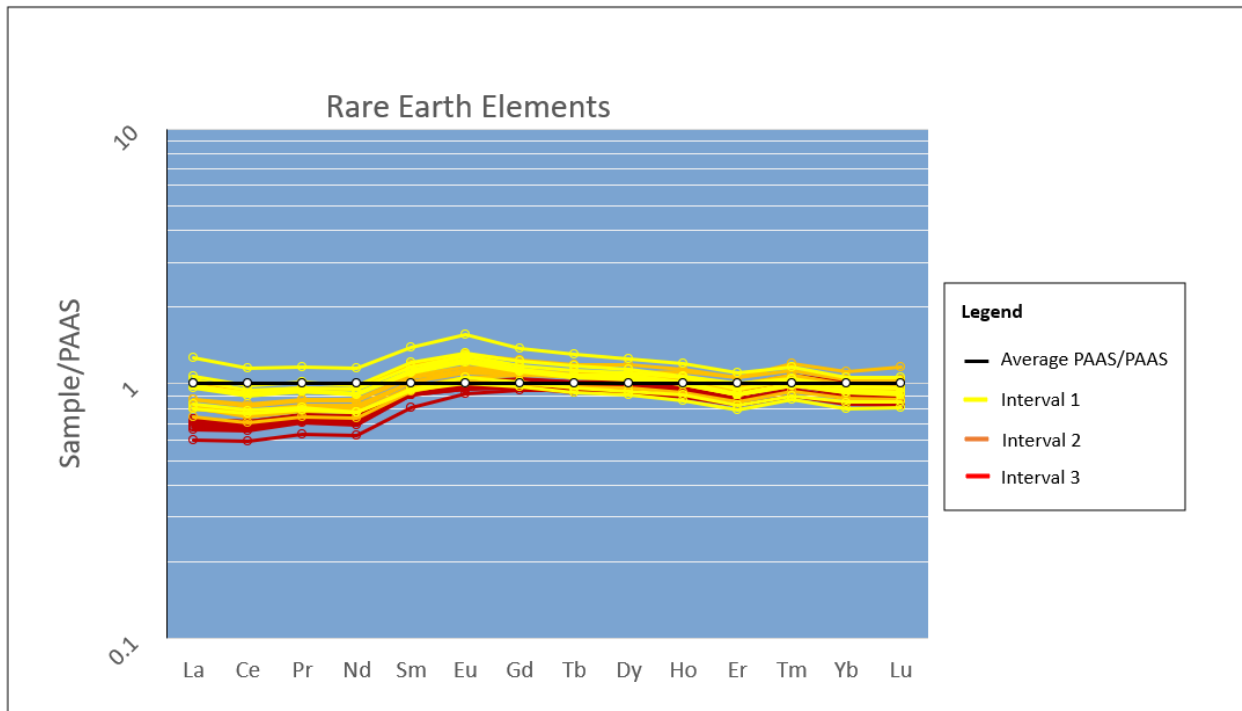
Figure 4. REE normalization to PAAS (Taylor and McLennan, 1985). Black line represents average PAAS normalized by PAAS.
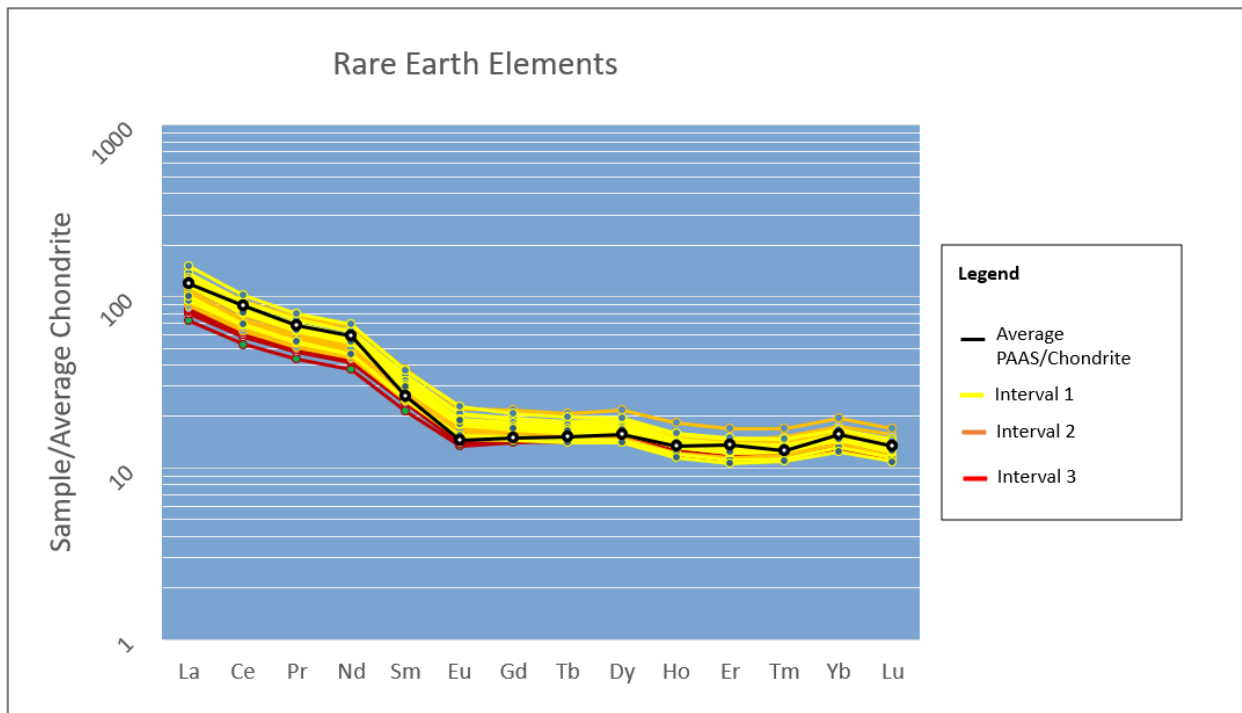
Figure 5. REE normalization to Chondrite (McLennan, 1989). Black line represents average values for PAAs normalized by average Chondrite.
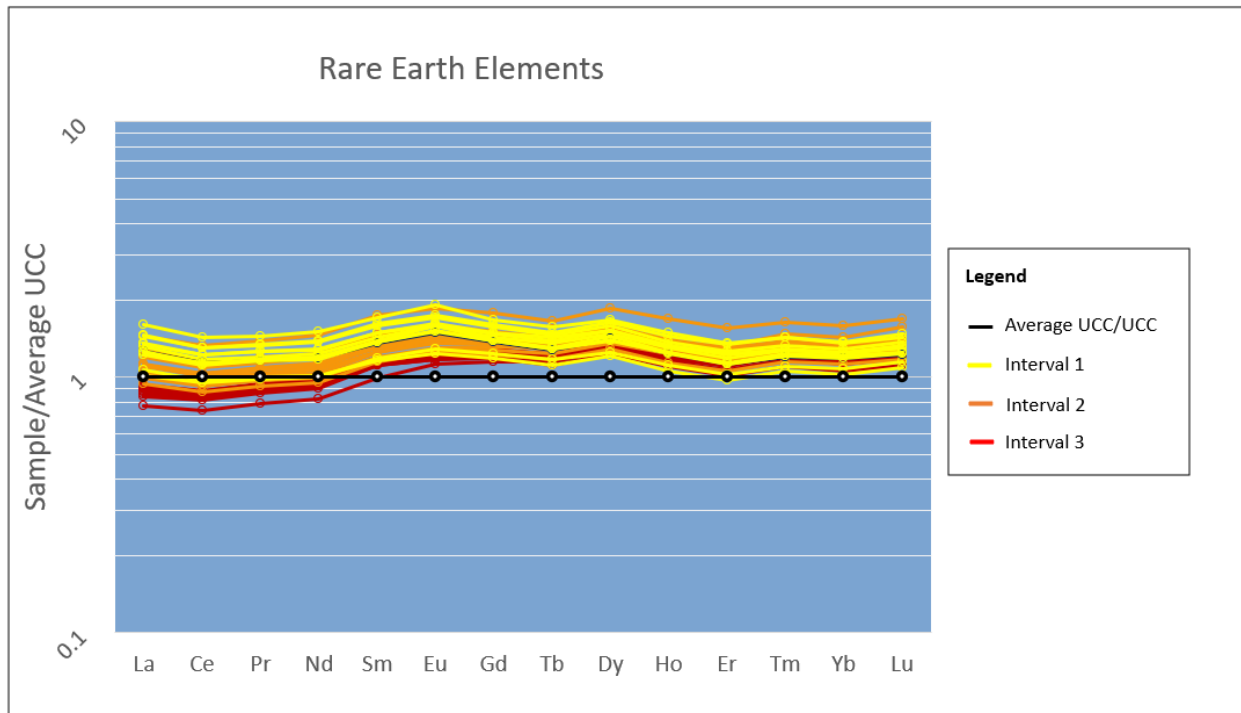
Figure 6. REE normalization to UCC (Taylor and McLennan, 1981). Black line represents average UCC normalized by UCC.

Provenance tracing

The initial phase in provenance tracing involved calculating elemental ratios to track detrital minerals at each interval, aiming to identify any alterations in the values that might signify a change in the source material. Tables 1, 2, and 3 show the results of trace and REE averages. The results were compared with a PAAS signature (Taylor and McLennan, 1985) marked as a pink star, with the East Antarctic mudstones (Light and Passchier, 2023) marked as a purple star, a WARS signature (Aviado et al., 2015) marked as a dark blue triangle, and to sediments exposed in the Antarctic Peninsula (Joseph, 2023) marked as a light blue triangle to compare geochemical signatures.

A plot of Th/Sc vs Zr/Sc was generated to assess whether the samples showed the effects of sediments recycling (McLennan et al. 1993). The compositions of samples across all intervals

exhibit a remarkable similarity, indicating a consistent source rock. Zr/Sc ratios range from 13 to

19, while Th/Sc ratios vary between 0.4 to 0.6. Although CRP-1 and CRP-2A values closely

resemble each other, they exhibit a similar signature to the Antarctic Peninsula sediments and

slight depletion in Th relative to Zr compared to those in the PAAS and East Antarctic

mudstones (Fig. 7).
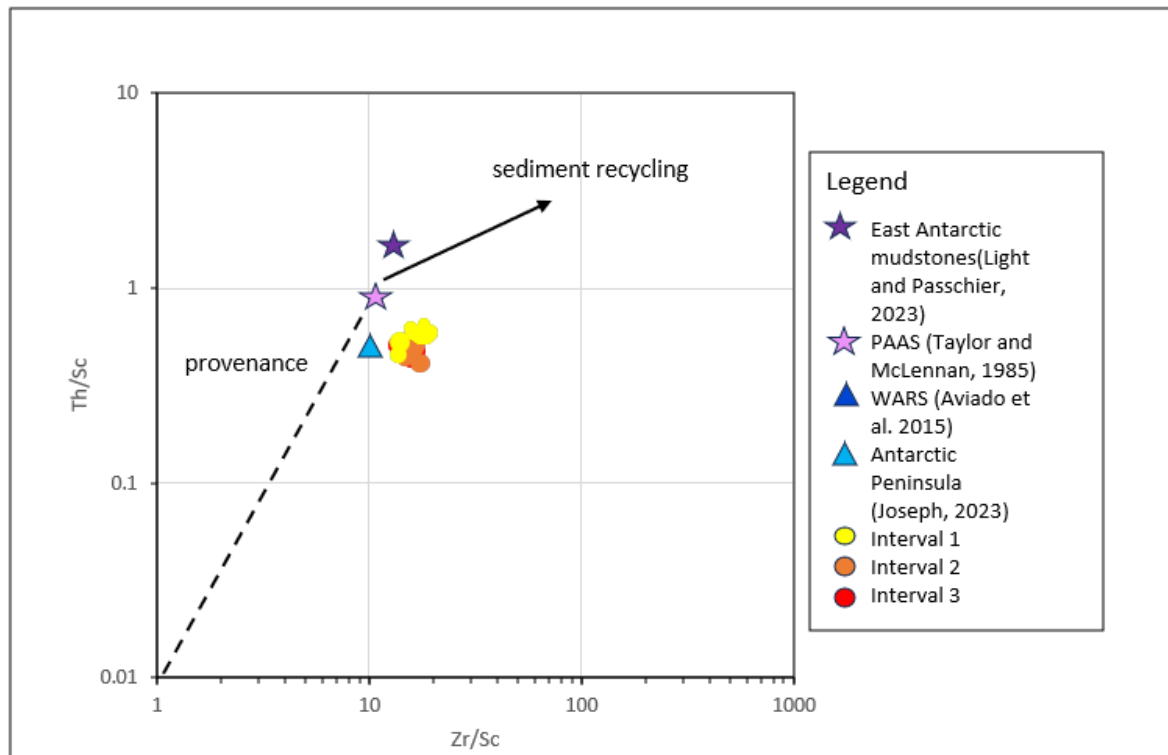
Figure 7. Th/Sc Th/Sc vs Zr/Sc ratios plot for sediment recycling (McLennan et al 1993). East Antarctic mudstones (Light and Passchier, 2023) marked as a purple star, PAAS signature (Taylor and McLennan, 1985) marked as a pink star, Antarctic Peninsula sediments (Joseph, 2023) marked as a light blue triangle, and WARS signature (Aviado et al., 2015) marked as a dark blue triangle. Dark blue triangle is missing due to the absence of Sc information on the WARS signature.

La/Th vs Hf plot was produced for tectonic setting discrimination (Floyd and Leveridge,

1987). The samples exhibit subtle compositional differences, with Hf ratios ranging from 6 to 9.

Simultaneously, La/Th ratios show variation between 2.9 and 4.6, with a depletion trend in the

ratios intensifying as the sample depth increases (Fig. 8). Notably, the values of the samples are

slightly higher than those of the PAAS and East Antarctic mudstones, indicating a slight

enrichment in La over Th, but similar values to the Antarctic Peninsula sediments.
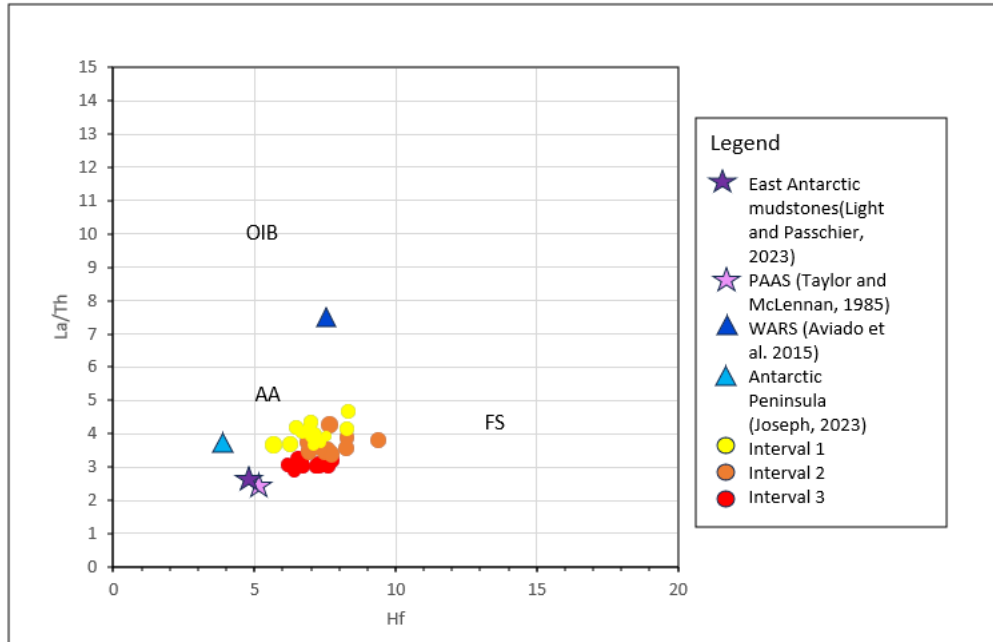
Figure 8. La/Th vs Hf ratio plot for tectonic discrimination (Floyd and Leveridge, 1087). Abbreviations: OIB – Oceanic Island basalt, AA – Andesitic Arc, FS – Felsic Source. East Antarctic mudstones (Light and Passchier, 2023) marked as a purple star, PAAS signature (Taylor and McLennan, 1985) marked as a pink star, Antarctic Peninsula sediments (Joseph, 2023) marked as a light blue triangle, and WARS signature (Aviado et al., 2015) marked as a dark blue triangle.

A plot of Th/U vs Th was created to illustrate the impact of U depletion caused by

metamorphism and chemical weathering, as discussed by McLennan et al. 1993. The Th/U ratios

exhibited a range of 3.6 to 5.6, with a minor enrichment in ratios observed at interval 1 (Fig. 9).

Concurrently, the Th values varied from 7 to 10, displaying remarkable similarity to the values

observed in the WARS and the PAAS.
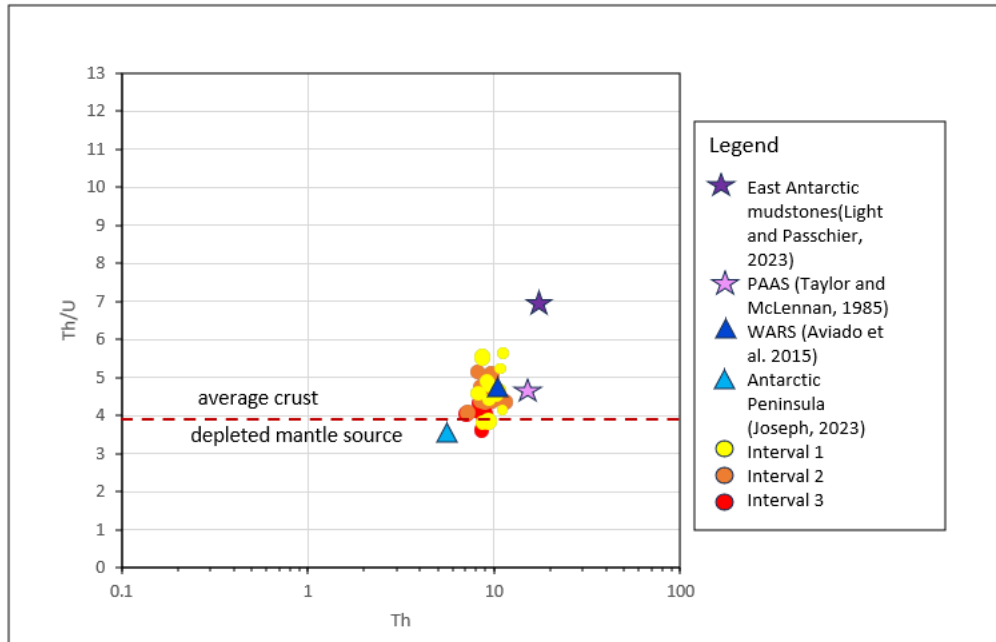
Figure 9.Th/U vs Th ratio plot for U depletion caused by metamorphism and chemical weathering (McLennan et al. 1993). East Antarctic mudstones (Light and Passchier, 2023) marked as a purple star, PAAS signature (Taylor and McLennan, 1985) marked as a pink star, Antarctic Peninsula sediments (Joseph, 2023) marked as a light blue triangle, and WARS signature (Aviado et al., 2015) marked as a dark blue triangle.

A plot of Nb/Ta vs Zr/Sm was generated to aid in identifying the tectonic setting, as outlined by Foley et al. (2002). Nb/Ta ratios displayed a range of 12 to 16, with a minor depletion observed at interval 3. In contrast, Zr/Sm ratios exhibited variability from 40 to 58 (Fig. 10). In general, the plot indicates values that closely resemble those of the PAAS and the Antarctic Peninsula sediments.
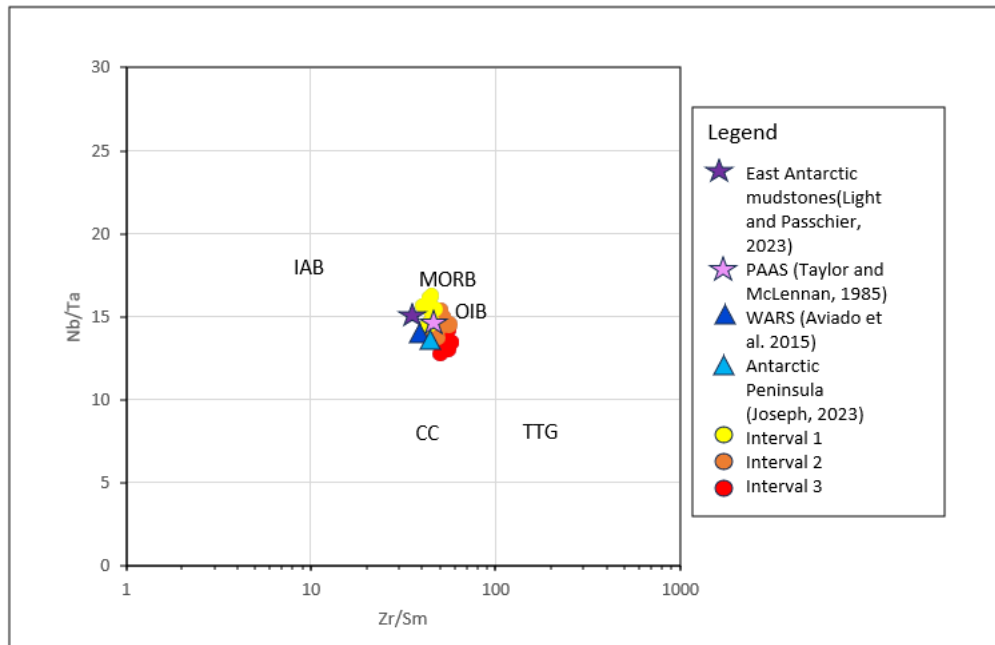
Figure 10. Nb/Ta vs Zr/Sm ratio plot for tectonic settings (Florey et al. 2000). Abbreviations: IAB – Island Arc Basalt, MORB – Mid- Ocean Ridge Basalt, OIB – Oceanic Island Basalt, CC – Continental Crust, TTG – Tonalite-Trondhjemite-Granodiorite. East Antarctic mudstones (Light and Passchier, 2023) marked as a purple star, PAAS signature (Taylor and McLennan, 1985) marked as a pink star, Antarctic Peninsula sediments (Joseph, 2023) marked as a light blue triangle, and WARS signature (Aviado et al., 2015) marked as a dark blue triangle.

A graph illustrating GdN/YbN vs Eu/Eu* was created to discern whether the samples were deposited in volcanic active tectonic settings (McLennan, 1989). The europium anomaly is expressed as Eu/Eu*, where Eu* is the anticipated europium value for the REE pattern:

$$Eu/Eu^* = Eu_N / (Sm_N * Gd_N)^{0.5}$$

'N' stands for chondrite-normalized values in the equation above.

The Eu/Eu* ratios ranged from 0.6 to 0.7, while GdN/YbN exhibited variability from 0.9 to 1.2, indicating a composition similar to a magmatic arc signature (Fig. 11). In general, the observed Eu/Eu* and GdN/YbN ratios falling within the range, suggest characteristics from active margin sediments similar to the PAAS and the Antarctic Peninsula sediments.
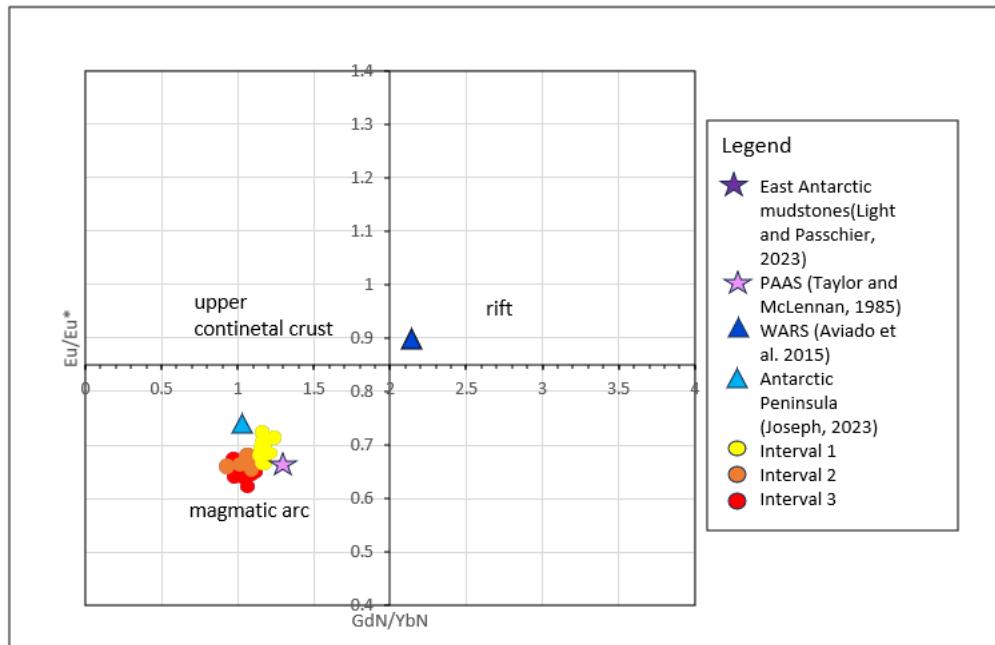
Figure 11. GdN/YbN vs Eu/Eu* ratio plot for volcanic active tectonic settings (McLennan, 1989). East Antarctic mudstones (Light and Passchier, 2023) marked as a purple star, PAAS signature (Taylor and McLennan, 1985) marked as a pink star, Antarctic Peninsula sediments (Joseph, 2023) marked as a light blue triangle, and WARS signature (Aviado et al., 2015) marked as a dark blue triangle. Purple star is missing due to the absence of GdN/Yb/N information on the East Antarctic mudstones signature.

In addition, a graph contrasting Th/Sc vs Eu/Eu* was generated to compare the samples to an East and West Antarctic provenance (Simoes-Pereira et al., 2018). Th/Sc ratios exhibited a range from 0.4 to 0.6 while Eu/Eu* ratios varied between 0.6 to 0.7 (Fig. 12). East Antarctic muddy sediments are expected to have a composition similar to PAAS. The samples displayed an Eu/Eu* ratio resembling that of PAAS and East Antarctic mudstones but with a significant depletion of Th similar to those present in the Antarctic Peninsula sediments.
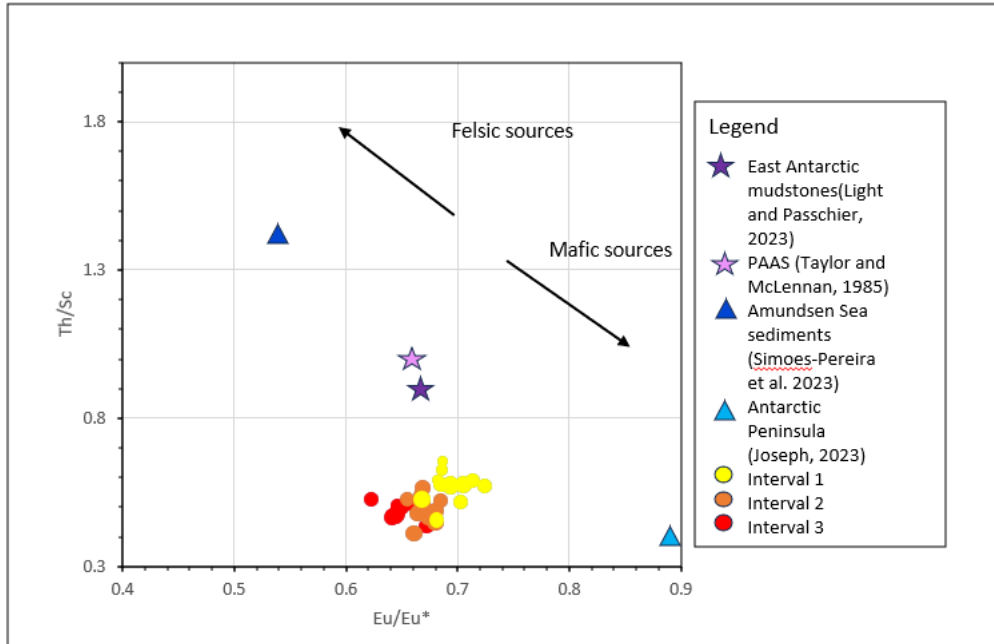
Figure 12. Th/Sc vs Eu/Eu* ratio plot for East and West Antarctic Provenance (Simoes-Pereira et al., 2018). East Antarctic mudstones (Light and Passchier, 2023) marked as a purple star, PAAS signature (Taylor and McLennan, 1985) marked as a pink star, Antarctic Peninsula sediments (Joseph, 2023) marked as a light blue triangle, and WARS signature (Aviado et al., 2015) marked as a dark blue triangle.

Grain Size Distribution Results

The grain size distributions for all intervals were graphed in Excel according to their particle size and the outcomes are presented in Table 4. Laser particle size analysis reveals that the sediments collected in intervals 1 of core CRP-1 and intervals 2 and 3 of core CRP-2A are consistently dominated by sandy silt and silty sand with a relatively low content of clay, results that are typical for diamictites matrix (Fig. 13).

Although individual samples within interval 1 display higher variability, the percentage of clay varied from 7.1% to 18.22%, silt from 33.77% to 71.37%, and sand from 21.30% to 54.10%. There is a general trend of increasing silt downcore. The lithological log for CRP-1 indicates that a significant portion of interval 1 primarily consists of sandstone with diamictites interbedded.

In samples at interval 2, the percentage of clay varied from 8.07% to 14.32%, silt from 37.44% to 50.17%, and sand from 35.57% to 51.54%, showing a trend of increasing sand downcore. CRP-2A lithology log classifies the samples as mostly mudstones and sandstones.

Within samples taken at interval 3, the percentage of clay varied from 11.53% to 15.41%, silt from 39.97% to 48.59%, and sand from 33.12% to 48.48%, indicating a similar pattern at interval 2 with an increasing trend in sand downcore. CRP-2A lithology log classifies this interval as thick layers of sandstone and diamictites interbedded.
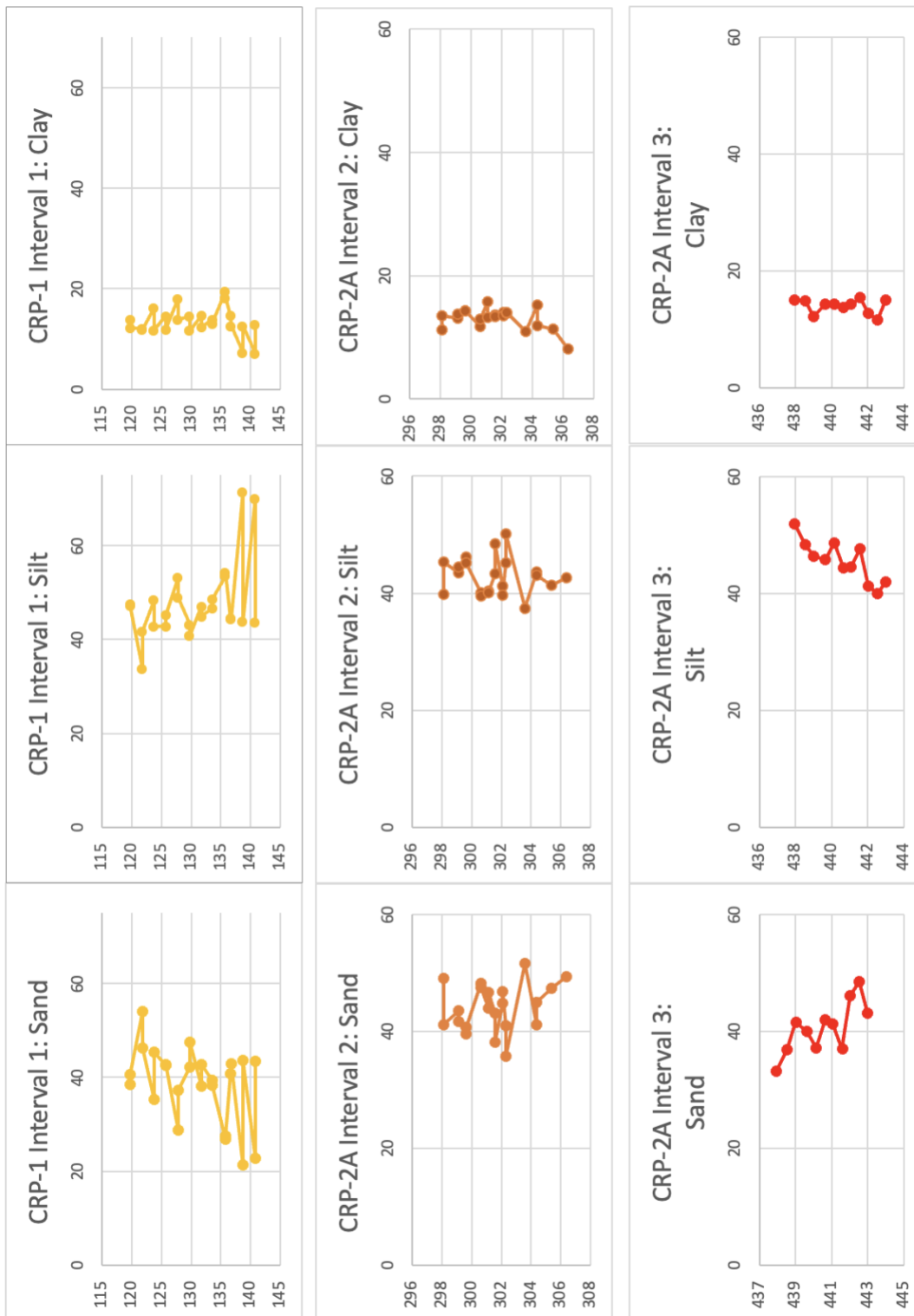
Figure 13. Grain Size distribution for CRP-1 and CRP-2A.

Discussion

Whole rock analyses via ICP-MS of 35 diamictite samples are interpreted to assess the provenance of each sample, enlightening on the origins and sources of these diamictites. Additionally, the grain size data is interpreted to discern the subglacial nature of the diamictites or the conditions under which these deposits were formed. The overarching goal of the study was to determine the presence of growing East and/or West Antarctic ice sheets during the Oligocene, contributing valuable information to our understanding of the paleoclimatic and glacial dynamics during this period.

Despite numerous studies, the understanding of the evolution of the West Antarctic Ice Sheet and its sub-ice geology remains quite undefined. The proposed CRP analyses expand our comprehension of the dynamics of the ice sheets and their potential existence in the Oligocene. The insights gained from this dataset have the potential to expand our geochemical knowledge of the geological terranes under the West Antarctic Ice Sheet.

The findings from the laser particle size analysis allow for inferences about potential environmental conditions at the time of sediment deposition. The results illustrated in Fig. 13 indicate a relatively consistent grain size across all intervals. This implies that within the early Miocene to the late Oligocene diamictite intervals, the depositional environment remained stable and aligned with the presence of subglacial tills.

ICP-MS geochemical analysis can be employed to determine the provenance of subglacial sediments. Even in minute quantities, trace and REE are compelling indicators of source rocks. In the results of normalized PAAS, most of the samples exhibit depletion of LREEs, along with a positive Eu anomaly and slight depletion of HREEs (Fig. 4). On the contrary, samples normalized to Chondrite show enrichment in LREEs, the presence of weak Eu anomaly, and

relatively modest enrichment in HREEs (Fig. 5). Similarly, under UCC normalization, the samples show enrichment in the LREE, a presence of a positive Eu anomaly, and enrichment in the HREE (Fig. 6). As per McLennan et al. (1993), an older upper continental crust displays a geochemical composition marked by a pronounced negative Eu anomaly and an enrichment of LREE. In contrast, a younger crust lacks a notable negative Eu anomaly and exhibits a lesser degree of LREE enrichment compared to an older upper crustal source. This makes a reasonable case to interpret that the REE enrichment and depletions relative to the PAAS, Chondrite and UCC show evidence of a younger crust.

The bivariate plots were compared against the PAAS (Taylor and McLennan, 1985) and to East Antarctic mudstones (Light and Passchier, 2023) for an East Antarctic signature, and to the WARS (Aviado et al. 2015), Antarctic Peninsula sediments (Joseph, 2023) and Amundsen Sea sediments (Simoes Pereira et al. 2018) for the West Antarctic signature. GdN/YbN vs Eu/Eu* (Fig. 11) was used to compare if the samples were deposited in a volcanic active tectonic setting (McLennan et al., 1989). The results showed a very similar composition to the PAAS and the Antarctic Peninsula sediments, indicating a magmatic arc signature. The Th/Sc vs Eu/Eu* plot was created to assess the provenance of the samples, where the PAAS and East Antarctic mudstones are the signature used for the East Antarctic provenance, and the Amundsen Sea and Antarctic Peninsula sediments are the signature used for the West Antarctic provenance. The results showed a different signature for both, with similar ratios for Eu/Eu* to the PAAS but a depletion of Th/Sc similar to those present in the Antarctic Peninsula sediments, assumed to be from a mafic source rock (Fig. 12). When compared to the results from Simoes Pereira et al. (2018), the signature of the CRP succession looks completely different from what we know of other parts of West Antarctica.

The Th/Sc vs Zr/Sc ratios of the CRP samples also show a similar composition to the Antarctic Peninsula sediments (Fig. 7), with similar values to the Th/Sc ratio, a sensitive indicator of bulk composition (Taylor and McLennan, 1985). Th/Sc and Zr/Sc are used to identify sediment recycling and sorting processes (McLennan et al. 1993). Th/Sc monitors the compositional variation of the source, while higher Zr/Sc ratios are associated with zircon enrichments due to sedimentary recycling. The trend of the CRP ratios represents sediments derived from intermediate to mafic igneous rocks that are less affected by sedimentary sorting and recycling.

Nb/Ta vs Zr/Sm ratios are used to discriminate the tectonic setting (Foley et al. 2002). The results show that the composition of the diamictite samples resembles the PAAS and the Antarctic Peninsula sediments composition, but also modern mid-ocean-ridge basalts or ocean-island basalts (Fig. 10).

La/Th vs Hf ratio plots also help understand the tectonic setting, the results show higher ratios than the PAAS but similar to the Antarctic Peninsula sediments. Based on Floyd and Leveridge (1987), the results appear to be from an andesitic arc source (Fig. 8). Th/U vs Th was created to illustrate the impact of U depletion caused by metamorphism and chemical weathering, as discussed by McLennan et al. (1993). Results showed a similar signature to the WARS and the PAAS, where most of the samples fall in the boundary between depleted mantle sources and upper crust signature, interpreted as a possible mix of sediments from an older and younger provenance (Fig. 9). In general, the geochemical results display a distinct signature that differs from the PAAS, the East Antarctic mudstones, and the WARS, prominently originating from a highly mafic igneous source, and not entirely compatible with old crust. Consequently,

these findings are construed as indicative of the sediment showing a signature different from an East Antarctic source and with a notable contribution from West Antarctica.

West Antarctica developed along the margin of Gondwana between the subducting Paleo-Pacific oceanic plate and the cratonic East Antarctic continent (Jordan et al. 2020). The main geological provinces of West Antarctica are: The Weddell Sea; the WARS and Marie Byrd Land; and the Antarctic Peninsula and Thurston Island. The Weddell Sea includes the oldest rocks in West Antarctica, experiencing minimal impact from marginal subduction. It shifted to its current position during the Jurassic on Gondwana's break-up associated with back-arc extension. The WARS and Marie Byrd Land followed as a subducting margin and magmatic arc outboard from East Antarctic Ross orogen. Subduction ceased during the Cretaceous. The Antarctic Peninsula and Thurston Islands exemplify a continental margin magmatic arc. Each of these West Antarctic provinces, or extensions thereof, could have contributed to the mafic signature in the CRP diamictites. Joseph (2023) examined samples from the Antarctic Peninsula, revealing a signature with Th/Sc and La/Th low ratios closely resembling those identified in the CRP succession. This represents the most comparable signature known to date.

In reconstructing glacial flow lines, several models have been proposed for the Last Glacial Maximum in the Ross Sea: the first one, a WAIS-dominated model, where a flow from WAIS to relatively narrow drainage along the western Ross Sea Coastline (Stuiver et al. 1981); the second one, a WAIS-EAIS balanced model, in which the confluence of West Antarctic ice and East Antarctic ice occurs in the central Ross Sea and both contributions are equivalent (Denton and Hughes, 2000); and a third one, a EAIS-dominated model in which WAIS strongly influences the eastern Ross Sea and the EAIS contributes with most of the ice to the central and western Ross Sea (Golledge et al. 2012). For these models, it is crucial to highlight that, according to Paxman

et al. (2019), during the Oligocene-early Miocene, the topography was significantly distinct from the current scenario, featuring a larger land area covered by the WAIS. According to the mentioned models and the evidence provided by this geochemical study, the proposed hypothesis is that the sediment source was mainly a contribution of the WAIS (Fig. 14), similar to the model proposed by Stuiver et al. (1981) that predicts a flow from the WAIS along the western and central Ross Sea coastline. Given the comparable composition of diamictite samples from the Miocene and Oligocene, it is logical to infer that the Antarctic Ice Sheet exhibited similar behaviors during these periods. It is also plausible to assume that the development and presence of the WAIS was initiated in the Oligocene.

The Antarctic Ice Sheets play a crucial role in Earth's climate system, and their dynamics are intimately connected to climate change. Understanding and monitoring the dynamics of ice sheets are critical for predicting future climate change scenarios. In a study by Duncan et al. (2022), the Oligocene is proposed as an extended period marked by global warming and ice-volume loss. During this time, the annual sea surface temperature in the Antarctic region is estimated to have ranged from 3-6°C. The retreat of the WAIS is attributed to a tectonically driven marine transgression with warm surface waters precluding ice sheet growth. Conversely, ice sheet expansion occurred when ocean temperatures further cooled during the Oligocene-Miocene transition. The presence of a WAIS in warmer conditions than today provides valuable insights into the ice sheet dynamics, enhancing our ability to project future climate change and rising global sea levels. The CRP succession has provided new perspectives on unraveling the origins of the Ross Sea sediments and the existence of a WAIS in warmer climates. However, the complex geology of Antarctica, the intricate dynamics of the ice sheets and the limited

information available emphasize the need for additional research to achieve more comprehensive

understanding.
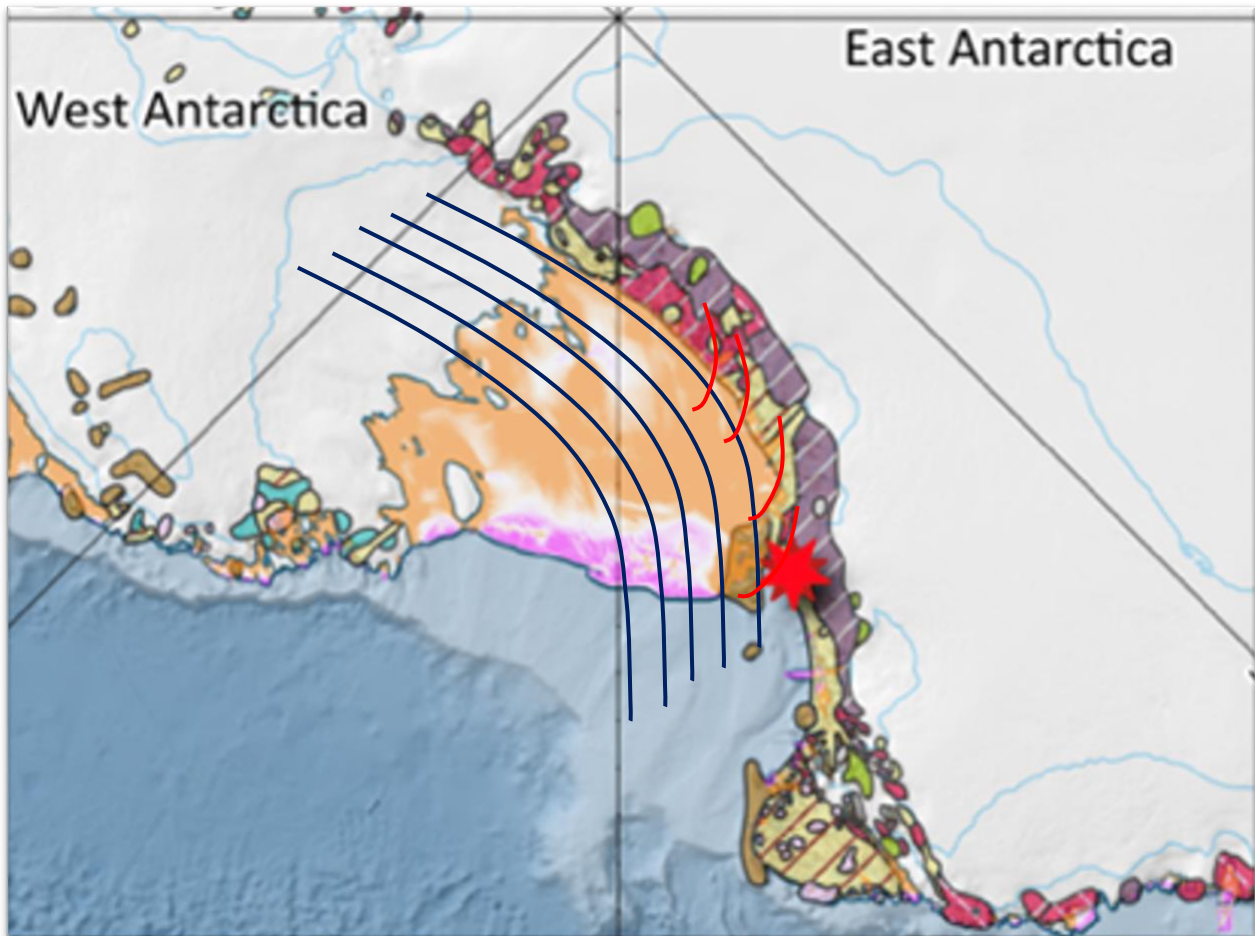
Figure 14. Interpretation of ice sheet expansion during the Miocene and Oligocene. Blue lines symbolize WAIS, whereas red lines symbolize EAIS.

Conclusion

The Cape Roberts Project was a collaborative effort involving multiple nations including Australia, Germany, Italy, the Netherlands, New Zealand, the United Kingdom, and the United States. Its primary objective was to extract a continuous core through 1200 meters of strata on the western side of McMurdo Sound, Antarctica. The CRP-2 and CRP-2A drilling site is located 14 km east of Cape Roberts, chosen to overlap with early Miocene strata cored in CRP-1 and to sample deeper into the east-dipping strata near the western margin of the Victoria Land Basin to investigate Paleogene climatic and tectonic history. CRP-2 was cored from 5 to 57 mbsf with a subsequent deviation leading to CRP-2A cored at the same location. CRP-2A reached a depth of 624 mbsf, providing access to strata dating back to 33.35 million years ago (Cape Roberts Project, 1999).

Based on the age model proposed by Florindo et al. (2005) and considering the composite depth of the CRP succession in relation to CRP-1 and CRP-2A, it is approximated that samples in interval 1 were deposited ~18-21 Ma, samples in interval 2 were deposited ~24 Ma, and interval 3 were deposited ~27-29 Ma. The purpose of this study was to collect data on 35 diamictite samples from the CRP succession to examine trace and Rare Earth Elements using ICP-MS and to interpret grain size analysis of (Martin and Passchier, 2010) to assess the hypothesis proposed by Sorlien et al. (2007) suggesting that the initial West Antarctic Sheet advance in the Ross Sea occurred during the Oligocene.

The proposed strategy was to compare REE results of the CRP succession to the Post Archean Australian Shale (PAAS) since East Antarctica and Australia have a very similar old upper crust composition as they were part of the same land mass in the supercontinent Gondwana. If the results showed a different ratio signature than the PAAS, similar to a young,

differentiated arc, it could validate that the provenance was a West Antarctic source. Overall, the geochemical results showed a similar signature for the Miocene and Oligocene, suggesting the Antarctic Ice sheet advanced and retreated in both periods in a similar pattern. The REE normalization to PAAS, Chondrite, and UCC showed a signature typical of a younger crust, the reason why it was interpreted the sediments come from a younger provenance.

Results from bivariate plots were compared to the PAAS, East Antarctic mudstones, and the WARS, showing in general a different provenance to all signatures. However, a pronounced depletion of Th was observed similar to the sediments present in the Antarctic Peninsula, suggesting a mafic source for the CRP samples. Several studies have suggested the presence of mafic rocks beneath the WAIS. Simoes Pereira et al. (2020) identified mafic rocks present in Pine Island and below the central portion of Thwaites glaciers, while Tinto et al. (2019) proposed the presence of magmatic arc blocks extending under the WAIS. Furthermore, Aviado et al. (2015) examined samples from the Ross Sea, Franklin and Beaufort Islands, and the northern Victoria Land discovering geochemical signatures akin to volcanic rocks through the WARS. The recent rifting and magmatic activity beneath the WAIS and its geochemical signature are different from the CRP samples.

Based on the results and some ice flow models proposed in the past, it was concluded that the main source of sediments was a West Antarctic source, possibly from similar rocks as those exposed on the Antarctic Peninsula. This major West Antarctic contribution suggests the presence of an expanding WAIS during the Oligocene. The samples in this study were compared with recognized regions in Antarctica, and a potential correlation was identified with samples gathered from the Antarctic Peninsula. However, there were slight discrepancies in geochemical signatures compared to our current understanding of Antarctic geology.

The possible existence of a WAIS in warmer conditions than those observed today offers valuable insights into ice sheet dynamics, climate change, and rising sea levels. However, further investigations are advised to enhance comprehension and interpretation of the current findings.

References

Anderson, J.B., 1999. Antarctic marine geology. Cambridge University Press, 1 - 57.

Aviado, K., Rilling-Hall, S., Bryce, J., and Mukasa, S., 2015. Submarine and subaerial kavas in the West Antarctic Rift System: Temporal record of shifting magma source components from the lithosphere and asthenosphere. AGU Publications.

Baker, P. E., Buckley, F., and Rex, D. C., 1977. Cenozoic Volcanism in the Antarctic. Royal Society of London, Biological Sciences, 279, 131-142.

Baranov, A., Tenzer, R., and Morelli, A., 2021. Updated Antarctic crustal model. Gondwana Research, 89, 1-18.

Berggren, W.A., Kent, D.V., Swisher III, C.C., Aubrey, M.P., 1995. A revised Cenozoic geochronology and biostratigraphy. In: Berggren, W.A., Kent, D.V., Aubrey, M.P., Hardenbol, J. (Eds.), Geochronology, Time Scales, and Stratigraphic Correlation. Society of Economic Paleontologists and Mineralogists, Special Publication, 54, 129– 212.

Bialas, R., Roger, W., Studinger, M., and Fitzgerald, P., 2007. Plateau collapse model for the Transantarctic Mountains – West Antarctic Rift System: Insights from numerical experiments. Geology 35, 687 – 690.

Boger, S. D., 2011. Antarctica before and after Gondwana. Gondwana Res, 19, 335-371.

Boulton, G., 1996. Theory of glacial erosion, transport, and deposition as a consequence of subglacial sediment deformation, Journal of Glaciology, 42(140), 43-62.

Brink, U.S., Hackney, R.I., Bannister, S., Stern, T.A., and Makovsky, Y., 1997. Uplift of the Transantarctic Mountains and the bedrock beneath the East Antarctic ice sheet. Journal of Geophysical Research, 102(621), 603 - 627.

Cande, S.C., Kent, D.V., 1995. Revised calibration of the geomagnetic polarity time scale for the
     Late Cretaceous and Cenozoic. Journal of Geophysical Research 100, 6093– 6095.

Cape Roberts Science Team, 1998. Initial Report on CRP-1, Cape Roberts Project, Antarctica.
     Terra Antarctica 5, 187.

Cape Roberts Project, 1999. Initial Report on CRP-2/2A. Terra Antarctica 6, ½.

Denton, G. H., & Hughes, T. J., 2000. Reconstruction of the Ross Ice drainage system,
     Antarctica, at the last glacial maximum. Geografiska Annaler, 82, 143–166.

Duncan, B., McKay, R., Levy, R., Naish, T., Prebble, J., Sangiorgi, F., Krishnan, S., Hoem, F.,
     Clowes, C., Dunkley Jones, T., Gasson, E., Kraus, C., Kulhanek, D., Meyers, S.,
     Moossen, H., Warren, C., Willmott, V., Ventura, G. and Bendle, 2022. Climatic and
     tectonic drivers of late Oligocene Antarctic ice volume. Nature Geoscience, 15, 819-825.

Fitzgerald, P.G., Sandiford, M., Barrett, P.J., and Gleadow, A.J.W., 1986. Asymmetric extension
     associated with uplift and subsidence in the Transantarctic Mountains and Ross
     Embayment. Earth and Planetary Science Letters, 81, 67 - 78.

Florindo, F., Wilson, G., Roberts, A., Sagnotti, L., and Verosub, K., 2005. Magnetostratigraphic
     chronology of a late Eocene to early Miocene glacimarine succession from the Victoria
     Land Basin, Ross Sea, Antarctica. Global and Planet Change 45, 207-236.

Florindo, F., Wilson, G., Roberts, A., Sagnotti, L., Verosub, K., 2001. Magnetostratigraphy of
     late Eocene-early Oligocene strata from the CRP-3 core, Murdo Sound, Ross Sea,
     Antarctica. Terra Antarctica, 8, 599-613.

Floyd, P. and Leveridge, B., 1987. Tectonic Environment of the Devonian Gramscatho basin.,
     south Cornwall: framework mode and geochemical evidence from turbiditic sandstones.
     Geological Society, 144, 531-542.

Foley, S., Tiepolo, M. and Vannucci, R., 2002. Growth of early continental crust controlled by melting of amphibolite in subduction zones. Nature, 417, 837–840.

Golledge, N. R., Christopher, J. F., Andrew, N. M., and Kevin, M. B., 2012. Dynamics of the last glacial maximum Antarctic ice sheet and its response to ocean forcing. Proceedings of the National Academy of Sciences, 40, 16, 52–56.

Goodge, J., 2020. Geological and tectonic evolution of the Transantarctic Mountains, from ancient craton to recent enigma. Gondwana Research, 80, 50-122.

Hanssen, V., 2011. Determining middle Miocene through Pliocene changes in provenance and basal ice conditions through sedimentological analyses of subglacial diamictites in AND-2A, Ross Sea, Antarctica.

Jordan, T., Riley, T., and Siddoway C., 2020. The geological history and evolution of West Antarctica.

Joseph, R., 2023. Antarctic Peninsula Ice Sheet Dynamics in the Pliocene from Sedimentological Interpretation of Ocean Drilling Program Site 1097. Montclair State University.

Kennett, J. P., 1997. Cenozoic evolution of Antarctic glaciation, the circum-Antarctic Ocean, and their impact on global paleoceanography. J Geophys Res 82, 3843–3860.

Konert, M., and Vandenberghe, J., 1997. Comparison of laser grain size analysis with pipette and sieve analysis; a solution for the underestimation of the clay fraction. Sedimentology, 44, p. 535.

Lavelle, M. 2000. Strontium-isotope Stratigraphy and age model for CRP-2/2-A, Victoria Land Basin, Antarctica. Terra Antarctica, 7, 611-620.

Marschalek, J., Zurli, L., Talarico, F., van de Flierdt, T., Vermeesch, P., Carter, A., Beny, F., Bout-Roumazeilles, V., Sangiorgi, F., Hemming, S., Perez, L., Colleoni, F., Prebble, J.,

van Peer, T., Perotti, M., Shevenell, A., Browne, I., Kulhanek, D., Levy, R., …IODP.

Expedition 374., 2021. A large West Antarctic Ice sheet explains early Neogene sea level

amplitude. Nature 600, 450-455.

Martin, L., and Passchier S., 2010. Basal ice conditions of the Antarctic Ice Sheet interpreted

from Oligocene through Pleistocene tills of the Cape Roberts drilling project.

Matsuoka, K., Skoglund, A., Roth, G., Pomereu, J., Griffiths, H., Headland, R., Herried, B.,

Katsumata, K., Le Brocq, A., Licht, K., Morgan, F., Neff, P., Ritz, C., Scheinert, M.,

…Melvaer, Y., 2021. Quantarctica, an integrated mapping environment for Antarctica,

the Southern Ocean, and sub-Antarctic islands. Environmental Modelling & Software.

McLennan, S. M., W. B. Nance, and S. R. Taylor, 1980. Rare earth element-thorium correlations

in sedimentary rocks, and the composition of the continental crust, Geochim.

Cosmochim. Acta, 44, 1833–1839

McLennan, S. M., 1989. Rare Earth Elements in sedimentary rocks; influence of provenance and

sedimentary processes. Mineralogy and Geochemistry, 21, 269-200.

McLennan, S. M., S. Hemming, D. K. McDaniel, and G. N. Hanson, 1993. Geochemical

approaches to sedimentation, provenance, and tectonics, in Processes, Controlling the

Composition of Clastic Sediments, edited by M. J. Johnsson, and A. Basu, Spec. Pap.

Geol. Soc. Am., 284, 21–40.

Mikhalsky, E., 2008. Age of the Earth's crust and the ND isotopic composition of the mantle

sources of East Antarctic complexes. Geochemistry International, 46, 168-174.

Nance, W. B., and Taylor, S. R., 1976. Rare Earth Element Patterns and crustal evolution.

Australian post-Archean sedimentary rocks.

National Science Foundation, 2020. McMurdo Station Records.

    www.nsf.gov/geo/opp/support/mcmurdo.jsp

Oregon Health and Science University, 2022. Elemental Analysis Core – ICP-MS as a

    Technique. https://www.ohsu.edu/elemental-analysis-core/icp-ms-technique

Passchier, S. and Krissek, L., 2008. Oligocene-Miocene Antarctic continental weathering record

    and paleoclimatic implications, Cape Roberts drilling Project, Ross Sea, Antarctica.

    Paleogeology, Palaeclim, Palaeeco, 260, 30-40.

Passchier, S., 2004. Variability in Geochemical Provenance and Weathering History of Sirius

    Group, Transantarctic Mountains: Implications for Antarctic Glacial History. Journal of

    Sedimentary Research.

Paxman J.G., Stewart, S.R., Hochmuth, K., Gohl, K., Bentley, M., Leitchenkov, G., and

    Ferraccioli, F., 2019. Reconstructions of Antarctic topography since the Eocene–

    Oligocene boundary, Palaeogeography, Palaeoclimatology, Palaeoecology, 535.

Simoes Pereira, P., van de flierdt, T, Hemming, S., Hammond, S., Kuhn, G., Brachfeld, S.,

    Doherty, C., and Hillenbrand C., 2018. Geochemical fingerprints of glacially eroded

    bedrock from West Antarctic Detrial thermochronology, radiogenic isotope systematics

    and trace element geochemistry in Late Holocene glacial-marine sediments. Earth

    Science Reviews, 182, 204-232.

Simoes Pereira, P., van de flierdt, T, Hemming, S., Hammond, S., Kuhn, G., Brachfeld, S.,

    Doherty, C., and Hillenbrand C., 2020. The geochemical and mineralogical fingerprint of

    West Antarctica's weak underbelly: Pine Island and Thwaites glaciers. Chemical

    Geology, 550.

Sorlien, C., Luyendyk, B., Wilson, D., Deccesari, R., Bartek, L., and Diebold, J., 2007. Oligocene development of the West Antarctic Ice Sheet recorder in eastern Ross Sea strata.

Stuiver, M., Denton, G. H., Hughes, T. J., and Fastook, J. L. ,1981. History of the marine ice sheets in West Antarctica during the last glaciation: A working hypothesis. In G. H. Denton, & T. Hughes (Eds.), The Last Great Ice Sheets, 319–439.

Taylor, S. R., McLennan, S. M., Armstrong, R. L, and Tarney, J., 1981. The composition and Evolution of the Continental Crust: Rare Earth Element Evidence from Sedimentary Rocks. Philosophical Transactions of the Royal Society London, 301, 381 – 399.

Taylor, S. R., and McLennan, S. M., 1985. The Continental Crust: Its Composition and Evolution, Blackwell, Malden, Mass.

Tinto, K.J., Padman, L., and Siddoway, C.S., 2019. Ross Ice Shelf response to climate driven by the tectonic imprint on seafloor bathymetry. Nat. Geosci. 12, 441–449.

Van der Meer, J., Menzies, J., and Rose, J., 2003. Subglacial till: The deforming glacier bed. Quaternary Science, 22, 1659-1685.

Watkins, D., Wise Jr, S., Villa, G., 2001. Calcareous nannofossils from Cape Roberts Project drill hole CRP-3, Victoria Land Basin. Antarctica. Terra Antarctica, 8, 229-3346.

Wilson, G., Roberts, A., Verosub, K., F., Florindo and Sagnotti, L., 2000. Magnetostratigraphy of Oligocene-Miocene glaciomarine strata from the CRP-2/2A core, McMurdo Sound, Ross Sea, Antarctica. Terra Antarctica, 7, 631-646.

Appendices

Final Average	442.94-98	442.50-53	442.00-03	441.55-58	441.04-07	440.60-64	440.10-13	439.60-64	438.98-439.01	438.50-53	437.91-94
45Sc	18.355	17.952	16.344	18.360	17.512	17.447	17.083	17.919	18.321	17.529	17.916
51V	116.607	113.849	105.280	125.657	115.277	115.119	116.620	122.587	120.119	118.307	120.637
53Cr	57.447	56.036	58.092	57.365	54.721	56.585	56.967	58.972	63.953	56.332	57.001
59Co	18.538	17.178	15.777	17.764	17.215	17.264	17.196	18.629	23.304	17.144	16.994
60Ni	29.772	26.784	26.718	29.805	27.407	26.757	27.547	32.773	28.797	34.617	28.534
71Ga	15.267	15.213	14.512	16.451	15.729	15.671	16.230	16.399	15.959	15.879	16.234
85Rb	79.620	78.508	70.578	91.890	79.401	81.701	88.588	89.957	81.032	85.542	88.041
86Sr	202.727	213.736	201.902	212.740	201.941	197.653	189.163	208.406	230.091	214.368	213.647
88Sr	201.565	213.801	201.143	211.844	200.601	197.713	189.649	207.694	228.794	214.297	212.668
89Y	29.634	27.742	26.635	27.361	26.670	26.638	24.354	25.636	28.082	27.321	26.446
90Zr	257.194	280.681	257.895	248.463	291.836	257.687	237.517	257.177	299.051	273.700	245.250
93Nb	13.190	14.778	12.879	15.437	13.879	14.575	15.221	15.283	15.462	14.985	15.387
133Cs	2.931	2.674	2.283	3.572	2.897	3.091	3.568	3.471	2.691	3.158	3.284
135Ba	377.011	386.560	365.204	420.494	379.316	380.320	393.291	413.588	409.865	401.891	411.673
137Ba	375.860	383.154	364.423	420.498	379.142	380.164	394.651	413.480	407.181	400.983	409.331
138Ba	372.142	379.720	362.183	417.250	374.184	376.729	389.795	409.915	405.103	398.212	406.741
139La	27.276	25.851	23.064	27.291	25.225	27.133	26.182	26.671	27.812	27.878	27.097
140Ce	54.640	53.245	47.282	56.100	51.924	55.071	53.702	54.295	56.368	56.757	55.715
141Pr	6.442	6.299	5.587	6.657	6.185	6.494	6.357	6.381	6.641	6.665	6.538
146Nd	24.522	24.080	21.370	25.257	23.419	24.672	23.986	24.189	25.116	25.479	25.033
147Sm	5.109	5.064	4.487	5.201	5.014	5.145	5.012	5.009	5.334	5.421	5.311
151Eu	1.051	1.048	0.993	1.114	1.041	1.063	1.028	1.068	1.085	1.063	1.084
153Eu	1.058	1.037	0.983	1.081	1.029	1.052	1.030	1.066	1.089	1.065	1.079
158Gd	4.759	4.631	4.364	4.859	4.590	4.659	4.484	4.554	4.831	4.814	4.699
159Tb	0.783	0.769	0.733	0.787	0.752	0.748	0.716	0.744	0.790	0.782	0.767
160Gd	4.853	4.700	4.418	4.908	4.656	4.715	4.509	4.614	4.874	4.878	4.797
163Dy	4.828	4.694	4.492	4.773	4.602	4.580	4.333	4.458	4.798	4.744	4.654
165Ho	1.022	0.972	0.964	0.992	0.955	0.948	0.879	0.923	0.994	0.984	0.936
166Er	2.808	2.651	2.584	2.667	2.598	2.546	2.339	2.462	2.679	2.622	2.557
169Tm	0.439	0.411	0.410	0.408	0.402	0.400	0.363	0.386	0.419	0.406	0.401
172Yb	2.862	2.638	2.612	2.674	2.641	2.600	2.336	2.476	2.728	2.638	2.528
175Lu	0.446	0.411	0.392	0.396	0.400	0.397	0.355	0.380	0.419	0.403	0.387
178Hf	6.639	7.284	6.548	6.402	7.598	6.590	6.173	6.692	7.759	7.153	6.414
181Ta	1.034	1.135	0.956	1.127	1.031	1.052	1.065	1.119	1.088	1.114	1.082
208Pb	18.470	14.194	13.898	15.657	13.669	13.276	13.315	19.396	13.584	16.449	15.592
232Th	8.572	8.425	7.142	9.403	8.344	8.694	8.525	8.777	8.666	9.219	9.072
238U	2.366	1.945	1.766	2.177	2.037	2.054	1.896	2.014	1.989	1.985	2.234

Table 1. Average trace and Rare Earth Elements for Interval 3.

Final Average	306.32-36	305.32-36	304.32-35	303.54-58	302.29-32	302.0710	301.55-58	301.07-10	300.5760	299.57-60	299.07-10	298.06-09
45Sc	18.355	17.952	16.344	18.360	17.512	17.447	17.083	17.919	18.321	17.529	17.916	17.473
51V	51.421	50.243	46.126	54.161	50.240	49.969	50.311	52.890	51.637	51.211	52.216	56.975
53Cr	97.336	95.346	89.816	103.091	95.236	95.355	96.833	101.286	97.177	97.222	99.356	110.898
59Co	44.468	43.263	43.906	44.260	42.152	43.258	43.788	45.566	48.511	43.158	43.781	45.172
60Ni	22.286	20.418	19.459	21.836	20.623	20.426	20.762	23.438	24.334	22.875	20.924	21.686
71Ga	25.015	22.971	22.539	25.414	23.708	23.130	23.932	27.359	23.272	28.206	24.636	25.076
85Rb	36.749	36.355	33.155	41.552	36.921	37.617	40.341	40.841	37.251	39.040	40.233	31.494
86Sr	121.115	124.052	114.509	132.262	120.591	120.621	122.219	129.633	128.600	128.411	130.118	125.417
88Sr	202.734	214.754	201.379	212.262	202.325	198.557	189.759	208.617	222.240	212.968	212.940	244.380
89Y	144.817	152.596	142.089	150.277	142.746	140.500	134.770	147.115	154.001	151.359	151.007	172.890
90Zr	105.611	112.242	103.734	101.144	115.160	103.663	95.481	102.858	117.477	109.409	99.490	122.177
93Nb	176.752	193.784	176.593	171.038	199.561	177.243	164.357	176.808	194.269	187.235	169.963	210.101
133Cs	9.832	10.879	9.395	11.575	10.303	10.795	11.382	11.326	10.642	11.003	11.470	12.746
135Ba	127.617	130.650	123.261	142.536	128.356	128.820	133.468	140.167	138.320	136.054	139.408	136.740
137Ba	376.944	386.762	365.632	422.172	379.935	381.010	395.007	413.847	396.399	401.406	412.390	411.743
138Ba	375.540	383.732	364.111	420.742	378.702	380.092	394.568	412.148	394.060	400.059	410.302	409.799
139La	257.700	262.365	249.956	287.865	257.945	260.934	268.851	281.976	266.675	274.365	281.532	282.412
140Ce	36.414	35.084	31.189	37.003	34.228	36.507	35.456	35.868	36.359	37.534	36.777	40.628
141Pr	38.714	37.946	33.547	39.904	37.008	39.035	38.213	38.498	38.150	40.069	39.562	42.397
146Nd	12.485	12.250	10.862	12.865	11.961	12.559	12.251	12.324	12.611	12.930	12.728	13.415
147Sm	18.085	17.821	15.808	18.690	17.360	18.222	17.717	17.859	17.704	18.873	18.584	19.672
151Eu	3.720	3.741	3.367	3.881	3.726	3.813	3.700	3.689	3.708	3.947	3.940	4.044
153Eu	1.057	1.052	0.998	1.117	1.040	1.060	1.029	1.070	1.051	1.059	1.084	1.162
158Gd	2.297	2.242	2.112	2.347	2.217	2.253	2.188	2.223	2.294	2.322	2.288	2.430
159Tb	3.440	3.351	3.156	3.496	3.318	3.360	3.234	3.286	3.350	3.455	3.399	3.612
160Gd	2.142	2.082	1.964	2.163	2.058	2.073	1.981	2.034	2.123	2.146	2.115	2.259
163Dy	4.848	4.711	4.435	4.839	4.626	4.665	4.454	4.550	4.692	4.814	4.748	5.160
165Ho	3.541	3.432	3.312	3.510	3.388	3.366	3.212	3.288	3.344	3.461	3.407	3.853
166Er	1.617	1.533	1.506	1.556	1.508	1.482	1.366	1.432	1.517	1.532	1.477	1.750
169Tm	2.029	1.914	1.875	1.923	1.878	1.833	1.699	1.771	1.832	1.865	1.845	2.199
172Yb	1.247	1.156	1.148	1.165	1.152	1.131	1.021	1.082	1.175	1.149	1.111	1.378
175Lu	2.069	1.917	1.903	1.937	1.922	1.889	1.687	1.798	1.862	1.884	1.826	2.307
178Hf	2.508	2.701	2.442	2.399	2.798	2.462	2.297	2.483	2.848	2.652	2.398	2.892
181Ta	4.762	5.259	4.690	4.649	5.392	4.752	4.492	4.858	5.252	5.146	4.654	5.568
208Pb	6.820	5.472	5.266	5.969	5.242	5.121	5.149	7.217	5.215	6.230	5.920	5.350
232Th	15.175	12.283	11.657	13.585	11.904	11.759	11.730	15.854	11.952	14.039	13.425	11.245
238U	6.482	6.303	5.370	7.064	6.271	6.488	6.348	6.552	6.138	6.801	6.809	5.458

Table 2. Average Trace and Rare Earth Elements for Interval 2.

Final Average	140.72-74	138.63-65	136.63-65	135.72-74	133.52-54	131.72-74	129.72-74	127.72-74	125.72-74	123.72-74	121.72-74	119.72-74
45Sc	18.263	16.860	18.370	17.785	17.507	18.267	18.041	16.024	16.118	16.166	16.378	15.091
51V	128.410	124.066	140.764	137.357	141.575	123.948	111.550	113.336	117.493	113.215	112.175	118.553
53Cr	86.697	75.320	83.014	82.136	79.756	70.387	71.354	66.361	70.997	74.720	72.158	70.043
59Co	21.488	18.479	20.243	19.243	18.322	17.280	16.433	16.630	16.317	16.846	17.084	15.500
60Ni	38.956	34.365	36.939	37.602	35.997	35.155	33.542	35.742	32.869	31.871	33.832	30.348
71Ga	19.264	18.763	19.432	19.744	19.865	18.659	17.456	17.887	17.719	17.770	17.175	17.526
85Rb	105.718	95.797	101.815	103.700	102.725	94.481	88.567	93.286	89.279	88.469	83.477	87.039
86Sr	299.443	325.823	337.223	298.048	368.450	296.739	255.595	280.911	287.267	294.776	239.557	313.053
88Sr	298.318	324.174	338.184	296.085	368.362	300.481	256.655	285.564	289.447	299.261	241.130	315.960
89Y	29.737	31.005	32.750	30.037	32.963	29.147	24.825	27.561	27.402	27.486	23.540	27.591
90Zr	289.695	303.711	330.397	280.140	335.527	257.044	246.558	264.358	283.121	286.787	227.521	282.020
93Nb	31.629	37.689	37.371	33.668	45.240	33.696	24.435	31.806	29.597	32.630	20.644	33.256
133Cs	2.868	2.291	2.468	2.848	2.483	2.394	2.185	2.419	2.167	2.161	1.998	2.045
135Ba	524.967	514.641	552.568	523.509	570.173	488.580	449.044	468.050	465.528	467.754	424.768	485.534
137Ba	526.292	519.077	556.163	525.343	573.211	488.897	448.111	470.222	468.663	471.343	426.109	489.098
138Ba	524.041	515.344	550.036	521.301	566.527	484.719	444.679	465.006	463.797	466.963	424.376	484.696
139La	40.492	43.474	44.045	40.973	48.225	39.611	30.374	37.775	37.524	36.828	31.921	37.763
140Ce	78.616	83.807	83.364	78.676	91.412	75.045	60.910	72.582	73.119	71.546	62.532	72.418
141Pr	8.995	9.486	9.506	8.966	10.275	8.468	6.994	8.224	8.337	8.239	7.104	8.281
146Nd	33.360	35.706	36.014	33.523	39.168	32.188	26.174	30.842	31.143	30.589	26.314	31.125
147Sm	6.695	7.131	7.284	6.721	7.725	6.429	5.316	6.097	6.161	6.166	5.255	6.238
151Eu	1.417	1.518	1.531	1.436	1.674	1.392	1.138	1.318	1.329	1.343	1.094	1.401
153Eu	1.398	1.492	1.538	1.410	1.702	1.400	1.139	1.304	1.324	1.349	1.087	1.394
158Gd	5.559	5.917	6.012	5.630	6.315	5.388	4.688	5.136	5.214	5.217	4.500	5.242
159Tb	0.890	0.936	0.954	0.913	1.009	0.869	0.749	0.819	0.822	0.824	0.715	0.834
160Gd	5.726	6.046	6.185	5.755	6.489	5.534	4.746	5.299	5.361	5.306	4.559	5.367
163Dy	5.338	5.596	5.768	5.331	5.887	5.155	4.385	4.941	4.869	4.917	4.254	5.045
165Ho	1.061	1.096	1.162	1.063	1.189	1.044	0.895	0.986	0.996	0.985	0.849	1.003
166Er	2.802	2.920	3.095	2.857	3.140	2.719	2.350	2.577	2.588	2.591	2.244	2.616
169Tm	0.425	0.438	0.472	0.423	0.471	0.421	0.364	0.397	0.400	0.402	0.350	0.409
172Yb	2.737	2.831	3.019	2.735	3.000	2.739	2.384	2.599	2.658	2.610	2.251	2.655
175Lu	0.425	0.440	0.471	0.417	0.460	0.418	0.369	0.392	0.399	0.396	0.349	0.401
178Hf	7.359	7.540	8.269	7.099	8.330	6.473	6.260	6.689	6.917	7.102	5.665	6.984
181Ta	2.061	2.353	2.297	2.138	2.806	2.155	1.578	2.060	2.021	2.111	1.423	2.133
208Pb	14.762	13.474	13.074	13.543	18.264	11.571	24.937	14.742	15.718	11.019	17.321	12.721
232Th	10.813	11.045	10.606	11.170	10.358	9.437	8.235	9.404	9.165	9.349	8.664	8.650
238U	2.062	2.661	2.270	1.981	2.275	1.965	1.794	2.128	1.869	2.432	1.564	2.271

Table 3. Average of Trace and Rare Earth Elements for Interval 1.

Table 4. Percentages of grain size data.

Sample	Sand	Silt	Clay
119.74	38.55274	47.63352	13.81374
119.74	40.58444	47.23116	12.1844
121.74	54.10723	33.77949	12.11328
121.74	46.26077	41.83736	11.90187
123.74	35.28859	48.43753	16.27388
123.74	45.46065	42.78626	11.75309
125.74	42.6061	42.83995	14.55395
125.74	42.78508	45.24662	11.9683
127.74	28.74635	53.21779	18.03586
127.74	37.22475	48.95151	13.82373
129.74	42.15169	43.2445	14.60382
129.74	47.48213	40.84997	11.6679
131.74	38.19995	47.11643	14.68362
131.74	42.7259	44.94567	12.32843
133.54	39.36164	46.68466	13.9537
133.54	38.28271	48.61008	13.10722
135.74	26.89594	53.53081	19.57325
135.74	27.48419	54.29012	18.22569
136.65	40.82197	44.51676	14.66127
136.74	42.96867	44.43566	12.59567
138.65	21.30665	71.37516	7.318193
138.65	43.60966	43.78637	12.60397
140.74	22.76023	70.08214	7.157639
140.74	43.41385	43.66083	12.92531
298.09	49.01898	39.75079	11.23024
298.09	41.13911	45.34369	13.5172
299.1	43.525	43.42682	13.04818
299.1	41.72203	44.51902	13.75895
299.6	39.54336	46.13238	14.32426
299.6	40.59816	45.12788	14.27396
300.6	48.13637	40.13272	11.73092
300.6	47.53264	39.57437	12.89299
301.1	43.93723	40.31836	15.7444
301.1	46.57009	40.1419	13.28802
301.58	43.06044	43.35677	13.58279
301.58	38.14358	48.45203	13.4044
302.1	44.72706	41.25484	14.0181
302.1	46.79195	39.68944	13.51861
302.32	40.97967	45.18051	13.83982

302.32	35.75372	50.1752	14.07109
303.58	51.54632	37.44902	11.00467
304.35	41.12855	43.64474	15.22672
304.35	44.94634	43.10172	11.95194
305.35	47.34165	41.28112	11.37723
306.36	49.36342	42.56407	8.072508
437.94	33.12867	51.82483	15.04649
438.53	36.78978	48.34937	14.86086
439.01	41.53083	46.32813	12.14104
439.64	39.91445	45.82698	14.25857
440.13	37.0807	48.59814	14.32116
440.64	41.8973	44.32198	13.78072
441.07	41.22346	44.5658	14.21074
441.58	36.98522	47.60267	15.41212
442.03	46.03969	41.17253	12.78779
442.53	48.48762	39.97957	11.53281
442.98	43.05944	42.00035	14.94022